Complete quasilinear model for the acceleration-driven lower hybrid drift instability and a computational assessment of its validity

G. V. Vogman● and J. H. Hammer●

Lawrence Livermore National Laboratory, *Livermore, California 94550, USA*

A complete quasilinear model is derived for the electrostatic acceleration-driven lower hybrid drift instability in a uniform two-species low-beta plasma in which current is perpendicular to the background magnetic field. The model consists of coupled nonlinear velocity space diffusion equations for the volume-averaged ion and electron distribution functions. Each species' diffusion coefficient depends on a time-evolving spectral density of the electric-field energy per unit volume and a time-evolving dispersion relation. The dispersion relation is expressed analytically in integral form without the use of asymptotic limits and applies to arbitrary distribution functions, so long as they can be expressed as a function of one velocity coordinate, e.g., $f(v_y)$ or $f(v_\perp)$. The quasilinear model conserves energy and is complete in that it fully describes the evolution of the distribution functions, including resonant and nonresonant particle-wave interactions, while accounting for distribution-function-dependent mixed-complex frequencies. The quasilinear diffusion model is solved numerically and self-consistently using a Crank-Nicolson temporal discretization and a second-order finite-volume velocity-space discretization. Numerical solutions are compared to nonlinear fourth-order accurate continuum kinetic Vlasov-Poisson simulations. Evolution of electric-field energy, growth rates, distribution functions, and diffusion coefficients are shown to be in agreement with Vlasov simulations. The quasilinear model is shown to predict anomalous transport terms, like resistivity and heating, to within a factor of order unity. Discrepancies between the quasilinear model and Vlasov simulations are assessed and attributed primarily to lack of damping in the quasilinear description and to the use of unperturbed-orbit susceptibilities in the linear theory dispersion relation. The results illuminate the predictive accuracy of the quasilinear model, place approximate bounds on its validity, and provide much needed vetting of quasilinear theory's ability to predict the nonlinear state of a microturbulent plasma.

I. INTRODUCTION

A common driver of kinetic instabilities is the relative drift between ions and electrons. Such instabilities give rise to nonlinear electromagnetic field fluctuations and particle-wave interactions that enhance macroscopic transport properties like resistivity and heating. This microturbulence-driven transport, also known as anomalous transport, is important because it can exceed classical collision-induced transport by orders of magnitude. Accurately characterizing anomalous transport is challenging because existing theoretical descriptions of nonlinear kinetic behavior, whether analytically or empirically derived, are not universally applicable and because computational investigations are limited by the computational cost of high-fidelity kinetic simulations. The lower hybrid drift instability (LHDI), which is caused by drift due to gradients [1,2] or acceleration [3,4] perpendicular to a background magnetic field, is a well-known nonlinear kinetic microturbulence phenomenon that gives rise to difficult-to-predict anomalous transport.

While LHDI microturbulence is important in magnetized fusion experiments [5,6] and in the magnetosphere [7–9], the motivation for the present investigation of the LHDI stems from pulsed power high energy density Z-pinch experiments [10] at the Z facility at Sandia National Laboratory.

These experiments, which rely on magnetically insulated transmission lines (MITLs) to deliver mega-amps of current to a Z-pinch load, can be unpredictably affected by collisionless plasmas produced at electrode surfaces of MITLs [11]. The MITL environment is characterized by a several-megavolt potential drop across the centimeter-scale anode-cathode gap and orthogonal magnetic fields that can range from zero to 200 Tesla over the course of a 100 ns current pulse [11,12]. See Fig. 1 for a simplified schematic of the configuration. The electric field within the pulsed power device is, in general, obtained by solving the full Maxwell equations and cannot be described as purely electrostatic or inductive. The low-density surface-produced plasmas are low-beta, such that the ratio of thermal pressure to magnetic pressure is much less than unity. These plasmas can bridge the anode-cathode gap [11,12] and are subject to time-dependent E × B drift, i.e., they undergo acceleration that induces a relative drift between ions and electrons. The resulting parasitic current is parallel to the electric field and orthogonal to the magnetic field, and, in principle, can be well-characterized, provided density is known and kinetic instabilities are absent. In the presence of LHDIs, plasma resistivity and heating are strongly affected by collisionless kinetic physics and therefore dynamics are not captured by classical resistive magnetohydrodynamic (MHD) models. Since experimental designs often rely on MHD
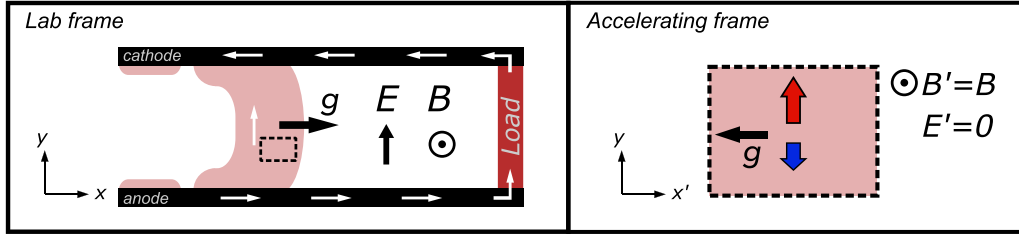
FIG. 1. A simplified schematic of a magnetically insulated transmission line (left), which is characterized by orthogonal time-dependent electric and magnetic fields. Collisionless low-beta plasmas produced at electrode surfaces bridge the anode-cathode gap, facilitate current pathways (denoted by white arrows), and are subject to time-dependent E × B drift. The rate of change of E × B velocity is denoted by the x-directed acceleration g. In a noninertial, i.e., accelerated frame comoving with the plasma (right), the electric field is zero and g points in the $-x$ direction. In both frames the acceleration induces a drift in the $+y$ direction for ions (denoted by red arrow) and in the $-y$ direction for electrons (blue arrow). To simplify theoretical analysis, the y direction of the accelerating-frame plasma is taken to be periodic.

simulations, LHDI-induced microturbulence effectively limits predictive modeling of power flow and load dynamics. The lack of predictive capability calls for reduced models [13,14] that can accurately translate nonlinear kinetic physics into resistivity and heating transport terms that can be included in MHD or multifluid simulations. The accuracy of existing treatments across the large range of possible plasma parameters is unknown but is something we hope to shed light on with this work.

The leading candidate theory for describing drift microturbulence is quasilinear theory. Originally developed in the 1960s [15–19], quasilinear theory is a weak turbulence theory that represents the aggregate effect of nonlinear kinetic dynamics in phase space by a coarse-grained diffusion in velocity space. The diffusion is nonlinear and the diffusion coefficient depends on a time-evolving dispersion relation. In a collisionless plasma, a diffusion description that encapsulates stochastic motion of particles through phase space can be applicable if there is a sufficiently broad spectrum of waves satisfying the Chirikov criterion [20] and/or a wave has sufficiently large amplitude [21]. For the theory to be applicable, the energy density of nonequilibrium oscillations must be small compared to thermal energy [17]. The theory further assumes that nonlinearities are small and yield small corrections to linear behavior, that mode coupling (i.e., wave-wave interaction) is negligible such that wave propagation can be described by linear theory, and that there is a separation of scales between a low-frequency background and high-frequency fluctuations. In effect, the theory captures nonlinearities in low-frequency average dynamics, but neglects nonlinearities in high-frequency dynamics [22].

In principle, if the nonlinear diffusion system can be solved self-consistently, then quasilinear theory provides a reduced model description for the effect of microturbulence on fluid transport—an important aim of turbulence studies more broadly [23]. Indeed, a common practical application of quasilinear theory is that it is used to derive microinstability-associated transport terms for single-fluid or multifluid plasma equations. Unfortunately, many applications of quasilinear theory, including for spatially uniform plasmas and for the LHDI [2], lack self-consistency because in solving the quasilinear equations they oversimplify dispersion relations, neglect nonresonant particle-wave interactions, and/or apply shortcuts to determine saturated-state

conditions. A notable exception is the self-consistent application of quasilinear theory presented in Ref. [24] for the bump-on-tail instability. A common simplification that leads to inconsistency is restricting the kinetic theory dispersion relation and/or its numerical solutions to Maxwellian distribution functions [2]. This precludes self-consistently solving the quasilinear governing equations, since the dispersion relation is not consistent with the time-evolving distribution function. Another inconsistency is commonly introduced when the velocity-space diffusion coefficient is evaluated in the small-growth-rate limit, which effectively ignores the effects of nonresonant (i.e., reversible) particle-wave interactions, which are known to contribute significantly to diffusion [25,26]. In the absence of self-consistent math, quasilinear models often rely on heuristic saturation rules that effectively guess saturated state plasma conditions and transport terms, without solving the quasilinear diffusion equations. Such rules have been informed by thermodynamic arguments [2], experimental studies, and dimensional arguments [27]. Consequently, the predictive accuracy and validity of self-consistent quasilinear models, let alone their simplified counterparts, remains a subject of debate, as explored in Refs. [24,28,29] for the bump-on-tail instability.

This paper shows that for the electrostatic acceleration-driven two-species LHDI, it is possible to derive and solve a mathematically complete self-consistent quasilinear model that avoids the aforementioned simplifications. The generalization is facilitated in part by examining the drift instability in the context of a uniform-density, uniformly accelerating plasma, with analysis performed in the noninertial plasma rest frame. Unique features of the derivation are that the associated dispersion relation is expressed in integral form, does not rely on asymptotic approximations, and applies to arbitrary velocity distribution functions—so long as they can be expressed as a function of one velocity coordinate: either velocity along the current flow direction, when distribution function dynamics are faster than gyromotion; or perpendicular velocity when distribution function dynamics are slower than gyromotion. This enables self-consistent time-dependent numerical solutions to the quasilinear diffusion model, which are not possible for fixed-distribution-function dispersion relations.

This paper is organized as follows. Section II describes the plasma configuration of interest and the associated

Vlasov-Poisson kinetic description. Section III presents a derivation of the linear theory kinetic dispersion relation for the acceleration-driven LHDI. Section IV presents a derivation of the quasilinear model for the acceleration-driven LHDI, describes the model's conservation properties, and presents quasilinear expressions for anomalous momentum and energy transport. Importantly, the model is shown to conserve energy, capture magnetized and unmagnetized species dynamics, and encapsulate both resonant and nonresonant particle-wave interactions. Section V describes the numerical solvers used to solve the dispersion relation and the quasilinear diffusion model, along with associated initial conditions. Section VI describes the nonlinear fourth-order accurate Vlasov-Poisson simulations, which are used to assess the accuracy of the quasilinear model. Section VII presents a detailed cross-comparison between quasilinear model numerical solutions and Vlasov-Poisson numerical solutions, specifically in terms of the time-evolving electric-field energy, spectral density of the electric-field energy, the structure of species distribution functions, the structure of diffusion coefficients, and anomalous transport. Energy balance is likewise assessed. Predictive capability is shown to be limited by the lack of damping mechanism in the quasilinear description and the fact that unperturbed-orbit species susceptibilities that comprise the dispersion relation eventually become inaccurate in the nonlinear stage of LHDI evolution, consistent with known limitations of plasma turbulence models [23]. Section VIII presents concluding remarks on the validity and predictive accuracy of the quasilinear model.

II. ASSUMPTIONS AND NONINERTIAL FRAME DESCRIPTION OF AN ACCELERATING KINETIC PLASMA

Far away from the load, which sits on axis of the Z machine, curvature effects are negligible and the current-carrying collisionless plasma can be analyzed in Cartesian slab geometry, as shown in Fig. 1. At LHDI-relevant scales, which are much smaller than experimental scales, the background magnetic field $\boldsymbol{B} = B_z\hat{z}$ and acceleration $\boldsymbol{g} = g_x\hat{x}$ associated with the time-dependent E × B drift can be approximated as being constant in space and time, implying a linearly increasing but spatially uniform electric field $\boldsymbol{E} = E_y\hat{y}$ in the laboratory frame. Since it is convenient to choose a frame in which this background electric field is zero, we proceed to carry out all theoretical analysis in an accelerating noninertial frame of reference, comoving with the plasma in the $\hat{x}$ direction, as shown in Fig. 1. The use of a noninertial frame of reference simplifies analysis and has precedent in other applications, including Rayleigh-Taylor instabilities in rotating plasmas [30], rotating tokamak plasmas [31], and imploding Z-pinches [32,33].

Considering only the most unstable modes, in which the perturbation wave number $\boldsymbol{k} = k_y\hat{y}$ such that $\boldsymbol{k} \cdot \boldsymbol{B} = 0$, the low-beta system can be treated as electrostatic and magnetostatic. Limiting to y-direction perturbations means that electric fields cannot develop in the $\hat{x}$ direction, which means that dynamics can be captured in 3D (y, v_x, v_y) phase space. In the accelerating frame, the plasma is in equilibrium with a relative y-directed drift between ions and electrons and experiences a fictitious gravitylike force in the $-\hat{x}$ direction, which

does not exist in an inertial frame. In the laboratory or other inertial frame, the drift would be identified as the polarization drift due to a time-varying electric field. The evolution of the plasma in the accelerating frame is described by the Vlasov-Poisson equation system

$$0 = \frac{\partial f_s}{\partial t} + \boldsymbol{v} \cdot \frac{\partial f_s}{\partial \boldsymbol{x}} + \left[\frac{q_s}{m_s}(\boldsymbol{E} + \boldsymbol{v} \times \boldsymbol{B}) - \boldsymbol{g}\right] \cdot \frac{\partial f_s}{\partial \boldsymbol{v}}, \quad (1)$$

$$-\nabla^2 \Phi = \frac{1}{\epsilon_0} \sum_s q_s n_s, \quad (2)$$

$$n_s = \int f_s d\boldsymbol{v}, \quad (3)$$

where ϵ_0 is the permittivity of free space, $f_s(\boldsymbol{x}, \boldsymbol{v}, t)$ is the probability distribution function, q_s is the particle charge, m_s is the particle mass, and n_s is the number density for species s. The electric field $\boldsymbol{E}$ can be expressed in terms of the electrostatic potential Φ, such that $\boldsymbol{E} = -\nabla\Phi$. This kinetic theory description provides a basis for quasilinear theory analysis, and for the linear theory analysis on which quasilinear theory relies.

III. LINEAR THEORY FOR THE ACCELERATION-DRIVEN LHDI

Expressing each variable in Eq. (1) in terms of an equilibrium quantity plus a small perturbation, e.g., $f_s = f_{s0} + f_{s1}$ with $f_{s1} \ll f_{s0}$, yields the linearized Vlasov equation,

$$\frac{\partial f_{s1}}{\partial t} + \boldsymbol{v} \cdot \frac{\partial f_{s1}}{\partial \boldsymbol{x}} + [\Omega_s(\boldsymbol{v} \times \hat{z}) - g\hat{x}] \cdot \frac{\partial f_{s1}}{\partial \boldsymbol{v}} = -\frac{q_s}{m_s}\boldsymbol{E}_1 \cdot \frac{\partial f_{s0}}{\partial \boldsymbol{v}}, \quad (4)$$

where $\Omega_s = q_s B_z/m_s$ is the species cyclotron frequency, whose sign depends on the species charge. The method of characteristics (see Ref. [34] for an example and Ref. [35] for a detailed description) is applied to solve for the perturbed distribution function. Equation (4) can be expressed in terms of a material derivative of df_{s1}/dt' along a characteristic phase space trajectory $(\boldsymbol{x}'(t'), \boldsymbol{v}'(t'), t')$ parameterized by t', such that

$$\frac{df_s(\boldsymbol{x}', \boldsymbol{v}', t')}{dt'} = -\frac{q_s}{m_s}\boldsymbol{E}_1(\boldsymbol{x}', t') \cdot \frac{\partial f_{s0}}{\partial \boldsymbol{v}'}. \quad (5)$$

Setting the end point of the trajectory to be where $t' = t$, $\boldsymbol{x}' = \boldsymbol{x}$, and $\boldsymbol{v}' = \boldsymbol{v}$ and integrating Eq. (5) with respect to t' over the interval $t' \in (-\infty, t]$ yields

$$f_{s1}(\boldsymbol{x}, \boldsymbol{v}, t) = -\frac{q_s}{m_s}\int_{-\infty}^{t} \boldsymbol{E}_1 \cdot \frac{\partial f_{s0}}{\partial \boldsymbol{v}'}dt'. \quad (6)$$

Assuming a waveform solution for f_{s1} and $\boldsymbol{E}_1$, such that

$$f_{s1} = \hat{f}_{s1}e^{i(\boldsymbol{k} \cdot \boldsymbol{x} - \omega t)}, \quad (7)$$

$$\boldsymbol{E}_1 = \hat{\boldsymbol{E}}_1 e^{i(\boldsymbol{k} \cdot \boldsymbol{x}' - \omega t')}, \quad (8)$$

and substituting Eqs. (7) and (8) into Eq. (6) yields

$$\hat{f}_{s1} = -\frac{q_s}{m_s}\int_{-\infty}^{t} \hat{\boldsymbol{E}}_1 \exp\left(i[\boldsymbol{k} \cdot [\boldsymbol{x}' - \boldsymbol{x}]\right.$$
$$\left. - \omega[t' - t]]\right) \cdot \frac{\partial f_{s0}}{\partial \boldsymbol{v}'}dt'. \quad (9)$$

If f_{s0} can be expressed in terms of constants of motion, then the integral in Eq. (9) can be simplified. To that end, let f_{s0} be a function of a single variable, U_s, defined to be a linear combination of the energy invariant $W_s = \frac{1}{2} m_s (v_x'^2 + v_y'^2) + m_s g x'$ and the rescaled canonical momentum invariant $P_{sy} = v_y'/\Omega_s + x'$ (see Ref. [36]), such that

$$U_s = W_s - m_s g P_{sy} = \frac{1}{2} m_s (v_x'^2 + v_y'^2) - \frac{m_s g v_y'}{\Omega_s}. \quad (10)$$

Importantly, U_s is independent of x', such that we consider spatially uniform equilibria. Using the chain rule, $\frac{\partial f_{s0}}{\partial v_y'} = \frac{\partial f_{s0}}{\partial U_s} \frac{\partial U_s}{\partial v_y'}$, and the fact that electric fields cannot develop in the $\hat{x}$ direction when perturbations are in the $\hat{y}$ direction, Eq. (9) can be expressed as

$$\hat{f}_{s1} = -q_s \frac{\partial f_{s0}}{\partial U_s} \int_{-\infty}^{t} \hat{E}_{1y} \exp(ik_y[y' - y]$$
$$+ i\omega_s[t - t']) \left(v_y' - \frac{g}{\Omega_s} \right) dt'. \quad (11)$$

In accordance with Eq. (1), the characteristic trajectory $(\mathbf{x}'(t'), \mathbf{v}'(t'), t')$ of a magnetized particle in phase space must satisfy a system of coupled ordinary differential equations,

$$\frac{d\mathbf{x}'}{dt} = \mathbf{v}', \quad (12)$$

$$\frac{d\mathbf{v}'}{dt} = \Omega_s \mathbf{v}' \times \hat{z} - g\hat{x}, \quad (13)$$

which are subject to the conditions $\mathbf{x}'|_{t'=t} = \mathbf{x}$ and $\mathbf{v}'|_{t'=t} = \mathbf{v}$. In Eqs. (12) and (13) it is assumed that the characteristic trajectory is not affected by the perturbation electric field, i.e., the trajectory is unperturbed. Solving the coupled system yields expressions for y' and v_y',

$$v_y' = \left(v_y - \frac{g}{\Omega_s} \right) \cos(\Omega_s[t - t']) + v_x \sin(\Omega_s[t - t'])$$
$$+ \frac{g}{\Omega_s}, \quad (14)$$

$$y' = -\left(\frac{v_y}{\Omega_s} - \frac{g}{\Omega_s^2} \right) \sin(\Omega_s[t - t']) + \frac{v_x}{\Omega_s} \cos(\Omega_s[t - t'])$$
$$- \frac{g(t - t')}{\Omega_s} - \frac{v_x}{\Omega_s} + y, \quad (15)$$

where g/Ω_s is the y-directed drift induced by the gravitylike force. The primed characteristic trajectory variables can be expressed in cylindrical velocity coordinates by setting θ to be the angle from the $+v_y$ axis and using the coordinate mapping

$$v_x = v_\perp \sin\theta, \quad (16)$$

$$v_y = v_\perp \cos\theta + \frac{g}{\Omega_s}. \quad (17)$$

In cylindrical coordinates, the characteristic trajectory variables of interest are

$$v_y' = v_\perp \cos\theta \cos(\Omega_s[t - t']) + v_\perp \sin\theta \sin(\Omega_s[t - t'])$$
$$+ \frac{g}{\Omega_s}, \quad (18)$$

$$y' = -\frac{v_\perp}{\Omega_s} \cos\theta \sin(\Omega_s[t - t']) + \frac{v_\perp}{\Omega_s} \sin\theta \cos(\Omega_s[t - t'])$$
$$- \frac{g(t - t')}{\Omega_s} - \frac{v_\perp \sin\theta}{\Omega_s} + y. \quad (19)$$

Substituting Eqs. (18) and (19) into Eq. (11), using trigonometric identities and the variable substitution $\tau = \Omega_s(t - t')$, and noting that $\partial/\partial U_s = (m_s v_\perp)^{-1} \partial/\partial v_\perp$, yields an expression for the perturbed distribution function for a magnetized species

$$\hat{f}_{s1}(k_y, \omega, v_\perp, \theta)$$
$$= -\frac{q_s}{m_s \Omega_s} \frac{\partial f_{s0}}{\partial v_\perp} \int_0^\infty \hat{E}_{1y} \exp\left[-\frac{2ik_y v_\perp}{\Omega_s} \cos\left(\theta - \frac{\tau}{2}\right) \right.$$
$$\left. \times \sin\left(\frac{\tau}{2}\right) + i\mathcal{W}_s \tau \right] \cos(\theta - \tau) d\tau, \quad (20)$$

where

$$\mathcal{W}_s = \frac{\omega}{\Omega_s} - \frac{k_y g}{\Omega_s^2}. \quad (21)$$

The choice of having f_{s0} be a function of the constant of motion in Eq. (10) effectively restricts applicability of the analysis to equilibrium distribution functions that are independent of the gyrophase. With additional mathematical manipulations, outlined in Appendix A, Eq. (20) and the linearized Poisson equation are used to obtain the implicit function dispersion relation $\epsilon(\omega, k_y) = 0$, i.e., the plasma dielectric, that relates mixed-complex frequency $\omega = \omega_R + i\omega_I$ and wave number k_y:

$$\epsilon(\omega, k_y) \equiv 1 + \sum_s \chi_s^{\text{mag}}(\omega, k_y) = 0, \quad (22)$$

where, for the magnetized species of interest, the susceptibility χ_s^{mag} is

$$\chi_s^{\text{mag}}(\omega, k_y) = \frac{\omega_{ps}^2}{\Omega_s^2} \int_0^{2\pi} \frac{\exp(i\mathcal{W}_s \phi)}{1 - \exp(2\pi i \mathcal{W}_s)} \sin(\phi) H_s(k_y, \phi) d\phi,$$

$$H_s(k_y, \phi) = \int_0^\infty f_{s0}(v_\perp) J_0\left(\frac{2k_y v_\perp}{\Omega_s} \sin\left[\frac{\phi}{2}\right] \right) v_\perp dv_\perp, \quad (23)$$

and where ω_{ps} is the species plasma frequency and $\mathcal{W}_s$ is given in Eq. (21).

In the derivation above, the frame of reference is noninertial in the x direction and additionally, for convenience, can include a uniform y-directed velocity $v_{y,\text{shift}}$. As expressed in Eq. (21), $v_{y,\text{shift}} = 0$ and each species has bulk y-directed velocity g/Ω_s. For an electron-ion plasma in a frame where the ions have zero y-directed velocity (we will refer to this as the ion "rest frame"), $v_{y,\text{shift}} = -g/\Omega_i$ and the frequency is Doppler shifted such that ω is replaced by $\omega - k_y v_{y,\text{shift}}$ in Eq. (21), resulting in $\mathcal{W}_i = \omega/\Omega_i$ and $\mathcal{W}_e = \frac{\omega}{\Omega_e} + \frac{k_y g}{\Omega_e \Omega_i} - \frac{k_y g}{\Omega_e^2}$.

In the limit where instability frequency is much larger than ion cyclotron frequency, ions can be treated as unmagnetized in the perturbed response. In this unmagnetized case the characteristic trajectories are straight lines and magnetic field effects are included in the equilibrium distribution function, but are neglected in perturbation f_{i1} because the Ω_i term in

Eq. (4) is much smaller than the $\partial f / \partial t'$ term and is thereby taken to be negligible. The resulting expressions for $\hat{f}_{i1}$ and the susceptibility for an unmagnetized ion species are

$$\hat{f}_{i1}^{\text{unmag}} = -\frac{iq_i}{m_i} \frac{1}{\omega - k_y v_y} \hat{E}_{1y} \frac{\partial f_{i0}}{\partial v_y}, \tag{24}$$

$$\chi_i^{\text{unmag}}(\omega, k_y) = \frac{\omega_{\text{pi}}^2}{k_y^2} \int_{-\infty}^{\infty} \frac{1}{\omega/k_y - v_y} \frac{\partial f_{i0}}{\partial v_y} dv_y. \tag{25}$$

Equations (24) and (25) are evaluated in the rest frame of the unmagnetized ion species.

While the analysis above admits any number of particle species, we will explore the acceleration-driven LHDI in the context of a two-species electron-ion plasma. We will consider two versions of the dispersion relation: one in which electrons and ions are both magnetized, as in Eq. (22), and one in which electrons are magnetized and ions are unmagnetized, such that

$$\epsilon(\omega, k_y) \equiv 1 + \chi_e^{\text{mag}} + \chi_i^{\text{unmag}} = 0. \tag{26}$$

Note that both the ion and electron susceptibilities in Eqs. (22) and (26) need to be evaluated in the same reference frame.

An advantageous feature of the susceptibility expression in Eq. (23) is that it is in integral form and does not involve infinite sums, which means that the dispersion relations of Eqs. (22) and (26) can be solved numerically to a high degree of accuracy without making asymptotic approximations and while fully accounting for gyroresonances. The utility of the integral form over the more common infinite-sum form, has been substantiated in other linear studies of finite-temperature kinetic instabilities [37–39]. By contrast, with few exceptions [37], dispersion relation derivations for gradient-driven LHDI often rely on summation-form expressions [1,2,40–42] of which only the first term is typically retained, thus restricting applicability to low-frequency ($\omega \ll \Omega_e$) long-wavelength modes [1,2,40,41,43]. Furthermore, the dispersion relations of Eqs. (22) and (26) [with susceptibilities defined in Eqs. (23) and (25)] do not impose commonly used asymptotic limits on the temperature ratio T_i/T_e, the frequency ratio ω_{pe}/Ω_e, or the ratio of wavelength to electron gyroradius. In contrast to dispersion relations in Refs. [2,5,44], the dispersion relations here are not restricted to Maxwellian distribution functions. Since the plasma under consideration is uniform, the local approximation used in LHDI analyses in Refs. [2,37,45], is not employed here. Importantly, the dispersion relations in Eqs. (22) and (26) capture scales associated with thermal speed and Larmor radius—features that limit growth rates, are characteristic of finite-temperature kinetic plasmas, and are missing in cold-fluid linear theory analysis, which is summarized in Appendix B.

IV. QUASILINEAR THEORY FOR THE ACCELERATION-DRIVEN LHDI

The quasilinear analysis of the acceleration-driven LHDI proceeds as follows. Let $\langle \cdot \rangle$ denote spatial average over one-dimensional volume L. Define distribution function f_s as the sum of a slowly evolving spatial average $f_{s0}(\boldsymbol{v}, t) \equiv \langle f_s \rangle = \frac{1}{L} \int_L f_s(\boldsymbol{x}, \boldsymbol{v}, t) d\boldsymbol{x}$ and a rapidly evolving portion $f_{s1}(\boldsymbol{x}, \boldsymbol{v}, t)$, whose spatial average $\langle f_{s1} \rangle$ is zero. Likewise, noting that for

the system of interest background electric field is zero and magnetic field and gravitylike force are constant, define $\boldsymbol{E} = \boldsymbol{E}_1$ with $\langle \boldsymbol{E}_1 \rangle = 0$, $\boldsymbol{B} = \boldsymbol{B}_0 = B_0 \hat{z}$, and $\boldsymbol{g} = \boldsymbol{g}_0 = g_0 \hat{x}$. Note that we have used the 0 and 1 subscripts to draw an analogy to the linear theory analysis presented in Sec. III, with the understanding that here the definitions of subscripted terms are different than in Sec. III. Substituting $f_s = f_{s0} + f_{s1}$ and these other definitions into Eq. (1), and taking the spatial average of the resulting expression yields an evolution equation for f_{s0},

$$0 = \left[\frac{\partial}{\partial t} + \boldsymbol{v} \cdot \frac{\partial}{\partial \boldsymbol{x}} + \left(\frac{q_s}{m_s} \boldsymbol{v} \times \boldsymbol{B}_0 - \boldsymbol{g}_0 \right) \cdot \frac{\partial}{\partial \boldsymbol{v}} \right] f_{s0}$$
$$+ \frac{q_s}{m_s} \left\langle \boldsymbol{E}_1 \cdot \frac{\partial f_{s1}}{\partial \boldsymbol{v}} \right\rangle. \tag{27}$$

Subtracting Eq. (27) from Eq. (1) yields an evolution equation for f_{s1},

$$0 = \left[\frac{\partial}{\partial t} + \boldsymbol{v} \cdot \frac{\partial}{\partial \boldsymbol{x}} + \left(\frac{q_s}{m_s} \boldsymbol{v} \times \boldsymbol{B}_0 - \boldsymbol{g}_0 \right) \cdot \frac{\partial}{\partial \boldsymbol{v}} \right] f_{s1}$$
$$+ \frac{q_s}{m_s} \boldsymbol{E}_1 \cdot \frac{\partial f_{s0}}{\partial \boldsymbol{v}} + \frac{q_s}{m_s} \frac{\partial}{\partial \boldsymbol{v}} \cdot (\boldsymbol{E}_1 f_{s1} - \langle \boldsymbol{E}_1 f_{s1} \rangle). \tag{28}$$

Quasilinear theory assumes that the last term in Eq. (28), which contains products of $\boldsymbol{E}_1$ and f_{s1}, is negligible. This means that the evolution of f_{s1} is linear in perturbed quantities and can thereby be described by linear theory. Consequently, the nonlinear evolution of the spatially averaged distribution f_{s0} [driven by the last term in Eq. (27)] is second-order in perturbed quantities. Another consequence of the assumption is that mode-coupling and three-wave interactions are neglected.

The only nonlinear contribution to the evolution of the background distribution function f_{s0} is the last term in Eq. (27); however, the spatial and velocity derivative terms in the square brackets are not necessarily negligible and whether they are important can depend on the details of the physics of interest. If spatial variation is sufficiently small (i.e., the background distribution function is close to uniform), then the $\partial/\partial \boldsymbol{x}$ term in Eq. (27) can be neglected. If any v_x-drift is negligible compared to v_y-drift, then the $\boldsymbol{g}_0$ term can also be neglected. If timescales of interest are much shorter than a gyroperiod, as would be the case for unmagnetized species, then $\boldsymbol{B}_0$ term in Eq. (27) can be neglected. The nonlinear dynamics of the spatially averaged distribution function in this case are governed by

$$\frac{\partial f_{s0}}{\partial t} = -\frac{q_s}{m_s} \left\langle E_{1y} \frac{\partial f_{s1}}{\partial v_y} \right\rangle. \tag{29}$$

Equation (29) can be rewritten as a velocity-space diffusion equation, as shown below.

For magnetized species, if the growth rates do not significantly exceed a species' gyrofrequency, then on timescales of order the gyroperiod and characteristic wave period, the spatially averaged distribution functions can be approximated as being constant and independent of the gyrophase [19]. Thus, Eq. (27) reduces to Eq. (29) for the magnetized species as well, where $f_0(v_x, v_y)$ can be replaced by $f_0(v_\perp)$ through the coordinate transformations in Eqs. (16) and (17) and f_0 is independent of gyrophase θ. In effect, for magnetized species, it is assumed that the mean diffusion time for a given species is

greater than a gyroperiod. This is consistent with magnetized-ion linear theory analysis in Sec. III, where it was assumed that equilibrium distribution functions are independent of gyrophase [see Eq. (20)]. The validity of these assumptions is assessed in Sec. VII C.

To rewrite Eq. (29) as a diffusion equation, real-valued quantities E_{1y} and f_{s1} in Eq. (29) are expressed as inverse Fourier transforms of $\hat{E}_{1k}^*(k_y, t)$ and $\hat{f}_{s1}(k_y, \boldsymbol{v}, t)$ with $\hat{f}_{s1}$ given by Eq. (20). Making use of the fact that for real-valued E_{1y}, conjugate symmetry properties

$$E_{1k}(k_y) = \hat{E}_{1k}^*(-k_y), \tag{30}$$

$$\omega_R(-k_y) = -\omega_R(k_y), \tag{31}$$

$$\omega_I(-k_y) = \omega_I(k_y) \tag{32}$$

hold, and also noting that in $(v_\perp, \theta)$ velocity space $\frac{\partial f_{s1}}{\partial v_y} = \frac{\partial f_{s1}}{\partial v_\perp} \cos\theta - \frac{\partial f_{s1}}{\partial \theta} \frac{\sin\theta}{v_\perp}$ yields the one-dimensional velocity-space diffusion equation for magnetized species

$$\frac{\partial f_{s0}}{\partial t} = \frac{1}{v_\perp} \frac{\partial}{\partial v_\perp} \left(v_\perp D_{vs}^{\text{mag}} \frac{\partial f_{s0}}{\partial v_\perp} \right), \tag{33}$$

with diffusion coefficient

$$D_{vs}^{\text{mag}}(v_\perp) = \frac{q_s^2}{m_s^2 \Omega_s \epsilon_0} \int_{-\infty}^{\infty} D_{vsk}^{\text{mag}}(v_\perp, k_y) dk_y,$$

$$D_{vsk}^{\text{mag}}(v_\perp, k_y) = \mathcal{E}_k \int_0^{2\pi} \text{Re}\left[\frac{\exp(i\mathcal{W}_s \phi)}{1 - \exp(2\pi i \mathcal{W}_s)} \right]$$

$$\times \left[J_0\left(\frac{2k_y v_\perp}{\Omega_s} \sin\left[\frac{\phi}{2} \right] \right) \cos(\phi) \tag{34} \right.$$

$$\left. - J_2\left(\frac{2k_y v_\perp}{\Omega_s} \sin\left[\frac{\phi}{2} \right] \right) \right] d\phi,$$

with $\mathcal{W}_i = \omega / \Omega_i$ and $\mathcal{W}_e = \frac{\omega}{\Omega_e} + \frac{k_y g}{\Omega_e \Omega_i} - \frac{k_y g}{\Omega_e^2}$ in the ion rest frame. For a given wave number k_y and distribution function f_{s0}, mixed-complex frequency $\omega = \omega_R + i\omega_I$ is obtained by solving the dispersion relation in Eq. (22) with susceptibilities defined in Eq. (23). In Eq. (34), $\mathcal{E}_k$ is the spectral density of the electric-field energy per unit volume and is defined as

$$\mathcal{E}_k = \frac{1}{2\pi L} \frac{1}{2} \epsilon_0 |\hat{E}_{1k}(k_y, t)|^2, \tag{35}$$

and its evolution depends on the time-evolving growth rate ω_I, such that

$$\frac{\partial \mathcal{E}_k}{\partial t} = 2\omega_I \mathcal{E}_k. \tag{36}$$

$\mathcal{E}_k$ is related to the total electric-field energy density $\mathcal{E}$ in the system by Plancherel's theorem, such that

$$\mathcal{E} = \frac{1}{L} \int_{-\infty}^{\infty} \frac{1}{2} \epsilon_0 |E_y|^2 dy = \frac{1}{2\pi L} \int_{-\infty}^{\infty} \frac{1}{2} \epsilon_0 |\hat{E}_{1k}(k_y, t)|^2 dk_y. \tag{37}$$

In the limit $g \to 0$ in $\mathcal{W}_e$, the integral-form diffusion coefficient in Eq. (34) can be shown to match the infinite-sum form of the diffusion coefficient in Ref. [19] for perpendicularly propagating waves in a nonaccelerating magnetized plasma. Just as with the linear dispersion relation, the integral form

facilitates accurate numerical evaluation without asymptotic approximations. The diffusion coefficient weakly depends on the distribution function f_{s0} through ω. Notably, the diffusion coefficient in Eq. (34) is zero unless growth rate $\omega_I > 0$.

Similarly, using Eq. (29), inverse Fourier transforms, and the definition of $\hat{f}_{s1}$ in Eq. (24) yields the well-known one-dimensional velocity-space diffusion equation for unmagnetized ions

$$\frac{\partial f_{i0}}{\partial t} = \frac{\partial}{\partial v_y} \left(D_{vi}^{\text{unmag}} \frac{\partial f_0}{\partial v_y} \right), \tag{38}$$

with diffusion coefficient

$$D_{vi}^{\text{unmag}}(v_y) = \frac{2q_i^2}{m_i^2 \epsilon_0} \int_{-\infty}^{\infty} D_{vik}^{\text{unmag}}(v_y, k_y) dk_y,$$

$$D_{vik}^{\text{unmag}}(v_y, k_y) = \frac{\mathcal{E}_k \omega_I}{(\omega_R - k_y v_y)^2 + \omega_I^2}, \tag{39}$$

with ω obtained by solving the dispersion relation in Eq. (26) with susceptibilities defined in Eqs. (23) and (25).

Due to the conjugate properties in Eqs. (30) to (32), all integrals over wave number that appear in Eqs. (34), (37), and (39) have integrands that are even functions of k_y. Consequently, integrals over wave-number domain $(-\infty, \infty)$ can be replaced by integrals over wave-number domain $[0, \infty)$, multiplied by two. Assuming that diffusion time is either significantly smaller than a gyroperiod (for unmagnetized species) or merely larger than a gyroperiod (for magnetized species) is ultimately what facilitates treating diffusion as one-dimensional in both cases. Notably, both Eqs. (33) and (38) encapsulate diffusion in velocity space associated with both resonant (irreversible) and nonresonant (adiabatic) wave-particle interactions. Accounting for nonresonant as well as resonant contributions is important for wholistic treatment of particle-wave interactions and for ensuring energy conservation [24–26,46].

The quasilinear diffusion description above captures dynamics of a multispecies plasma, such that the variables $f_{e0}, f_{i0}, \mathcal{E}_k, \omega(k_y)$ are self-consistently coupled and are all time-evolving. Importantly, the quasilinear description here admits arbitrary distribution functions, so long as they are a function of a single velocity coordinate (either $v_\perp$ or v_y). This stems from the fact that the dispersion relations can be, as described in Sec. V A, numerically solved for $\omega(k_y)$ given any smooth $f_e(v_\perp), f_i(v_\perp)$, and $f_i(v_y)$. By contrast, many quasilinear descriptions (including those for the gradient-driven LHDI [2,44,47,48]) are not truly self-consistent because they assume Maxwellian or bi-Maxwellian distribution functions when deriving or solving dispersion relations [2,47,49–51]. Such assumptions preclude a self-consistent time-dependent description because a Maxwellian-specific $\omega(k_y)$ does not reflect changes to the shape of the distribution function.

Conservation properties and anomalous transport

The velocity-space diffusion of the average background distribution function due to the acceleration-driven LHDI gives rise to momentum and energy transport, which can be evaluated explicitly by taking v_y-velocity moments of Eq. (29). This anomalous transport is inherently nonlinear and

is not captured by standard collisionality-based fluid descriptions. For the transport model to be practical, the quasilinear description must conserve momentum and energy. Here we explore transport and conservation properties of the quasilinear model and demonstrate that momentum and energy are, in fact, conserved. Note that the zeroth velocity moment of Eq. (29) is zero, implying mass is inherently conserved.

Taking the first v_y-velocity moment of Eq. (29) and multiplying through by species mass m_s yields an expression for the rate of change of a species' momentum density due to the action of acceleration-driven LHDI. In effect, the anomalous momentum transport is equivalent to a drag force per unit volume, F_{ds}, acting on species s:

$$F_{ds} \equiv \frac{\partial}{\partial t}(m_s n_s u_{sy}) = q_s \langle E_{1y} n_{s1} \rangle. \qquad (40)$$

From the definition of induced polarization in an isotropic medium (e.g., see Ref. [52]), $q_s n_s = -\nabla \cdot (\epsilon_0 \chi_s E)$, where χ_s is the species susceptibility—either for a magnetized or unmagnetized species. Linearizing this expression and assuming waveform solutions yields a relationship between perturbed number density n_{s1} and the perturbed electric field, such that $q_s \hat{n}_{s1} = -i k_y \epsilon_0 \chi_s \hat{E}_{1k}$. This relation is consistent with quasilinear estimates, in which nonlinear terms are second order in perturbed quantities [2]. Using this relation, applying Fourier transforms, and taking E_{1y} to be real, the species drag force per unit volume in Eq. (40) can be expressed as

$$F_{ds} = 2 \int_{-\infty}^{\infty} k_y \text{Im}[\chi_s] \mathcal{E}_k dk_y, \qquad (41)$$

where $\text{Im}[\cdot]$ denotes the imaginary part of the argument and $\chi_s = \chi_s(k_y, \omega)$ is evaluated at $\omega(k_y)$ solutions to the dispersion relation. Since for any (k_y, ω) pair that satisfies the dispersion relation, $\text{Im}[\chi_i] = -\text{Im}[\chi_e]$, it follows that $F_{di} = -F_{de}$, which means that the quasilinear model conserves momentum.

In a two-fluid description of an electron-ion plasma, the drag force per unit volume on electrons (which is equal and opposite to that on ions) can be expressed as $F_{de} = -\nu_{\text{anom}} m_e \langle n_e u_{ye} - n_i u_{yi} \rangle$, where ν_{anom} is the anomalous effective electron-ion collision frequency. Using this definition of electron drag and Eq. (41), one can solve for ν_{anom} and, by extension, for anomalous resistivity $\eta_{\text{anom}} = \nu_{\text{anom}} m_e/(q_e^2 n_e)$. Resistivity is of interest when quantifying current flow through a kinetic LHDI-unstable plasma.

Taking the second v_y-velocity moment of Eq. (29) and multiplying by $\frac{1}{2} m_s$ yields an expression for the anomalous species heating rate $\dot{W}_{Hs}$ (i.e., the rate of change of the species thermal energy density):

$$\dot{W}_{Hs} = \langle E_{1y} j_{sy1} \rangle. \qquad (42)$$

The linearized continuity equation relates the perturbed species current $j_{sy1} = q_s (n_s u_{sy})_1 = q_s \int f_{s1} v_y dv_y$ to perturbed number density, such that $\widehat{(n_s u_{sy})}_1 = (\omega'/k_y) \hat{n}_{s1}$, where ω' here is in a given species' rest frame. Using this relation, the polarization-based relationship between $\hat{n}_{s1}$ and $\hat{E}_{1k}$, the fact that E_{1y} is real, and Fourier transforms, the species heating rate is

$$\dot{W}_{Hs} = 2 \int_{-\infty}^{\infty} \text{Re}[-i(\omega - k_y u_{s0y}) \chi_s] \mathcal{E}_k dk_y, \qquad (43)$$

where $\text{Re}[\cdot]$ denotes the real part of the argument and u_{s0y} is the species equilibrium drift velocity in a given frame of reference so that in the ion rest frame $u_{i0y} = 0$ and $u_{e0y} = (\frac{g}{\Omega_e} - \frac{g}{\Omega_i})$.

In addition to the rate of change of electric-field energy density given by $\dot{\mathcal{E}} = 2 \int_{-\infty}^{\infty} \omega_I \mathcal{E}_k dk_y$ [i.e., Eq. (36) integrated over wave number], and the rate of change of species thermal energy density in Eq. (43), there is also a rate of change in the "gravitational energy density," i.e., the energy density associated with the gravitylike acceleration. This rate is given by

$$\dot{W}_g = -\sum_s m_s n_s g u_{sx} = \sum_s \frac{g}{\Omega_s} F_{ds}, \qquad (44)$$

where u_{sx} is the species x-directed velocity induced by y-directed drag, and the last equality in Eq. (44) uses force balance, such that $F_{ds} = -q_s n_s u_{sx} B_z$. Note that the y-directed species drift energy $W_{ys} = \frac{1}{2} m_s n_s u_{s0y}^2$ is constant in the model. The rate of change of kinetic energy density associated with x-directed drift, i.e., $\dot{W}_{xs} = \frac{\partial}{\partial t}(\frac{1}{2} m_s n_s u_{sx}^2)$, is fourth-order in perturbed quantities and is not accounted for in the model. Noting that $\text{Im}[\chi_i + \chi_e] = 0$ and $\text{Re}[\chi_i + \chi_e] = -1$ one can show that the sum of $\dot{\mathcal{E}}$, $\dot{W}_{Hi}$, $\dot{W}_{He}$, and $\dot{W}_g$ is zero, which means that the quasilinear model conserves energy.

Due to the conjugate symmetry properties in Eqs. (31) to (32), one can show that $\chi(-k_y, \omega(-k_y)) = \chi^*(k_y, \omega(k_y))$. Therefore, integrals over wave-number domain $(-\infty, \infty)$ that appear in Eqs. (41) and (43) and implicitly in Eq. (44) can be replaced by the integral over wave-number domain $[0, \infty)$, multiplied by two, such that $\int_{-\infty}^{\infty} \cdots dk_y = 2 \int_0^{\infty} \cdots dk_y$.

V. NUMERICAL SOLVERS FOR THE QUASILINEAR GOVERNING EQUATIONS

The governing equations of the quasilinear model for acceleration-driven LHDI—specifically the linear theory dispersion relation given in Sec. III and the coupled diffusion equation system given in Sec. IV, are solved numerically, as described in the following subsections.

A. Solving the dispersion relation

The dispersion relation for the acceleration-driven LHDI, as defined in Sec. III in Eq. (22) or in Eq. (26), can be solved directly to a numerical tolerance or can be solved approximately in the small-growth-rate limit. Both approaches require efficient and accurate evaluation of the integrals in Eqs. (23) and (25). Approaches for evaluating χ_s^{mag} and χ_s^{unmag}, solving the dispersion relation directly, and solving the dispersion relation approximately are described below.

Prior to solving the dispersion relation, it is convenient to evaluate susceptibilities in the ion rest frame and to nondimensionalize variables with respect to spatial scale $g/(\Omega_i \Omega_e)$ and temporal scale $(\Omega_i \Omega_e)^{-1/2}$. The ion rest frame is convenient since the real frequency for the instability falls between ion Bernstein wave modes. The choice of nondimensionalization facilitates making connections to cold-fluid theory (see Appendix B), in which $g/(\Omega_i \Omega_e)$ is the only spatial scale in the system, and to gradient-driven LHDI theory [2,37], in which the lower hybrid frequency ω_{LH} is often evaluated

in the high density limit such that $(\omega_{pe}/\Omega_e)^2 \gg 1$, wherein $\omega_{\mathrm{LH}} = (\Omega_i \Omega_e)^{1/2}$. Nondimensional variables will be denoted by tilde $\tilde{}$, such that $\tilde{k}_y = k_y g/|\Omega_i \Omega_e|$ and $\tilde{\omega} = \omega/(\Omega_i \Omega_e)^{1/2}$.

In general, it is desirable to solve the dispersion relation directly for mixed-complex frequency $\tilde{\omega} = \tilde{\omega}_R + i\tilde{\omega}_I$, without invoking simplifying assumptions. This can be achieved so long as the integrals in Eqs. (23) and (25) are computable. The integrals that appear in the magnetized-species susceptibility χ_s^{mag} [see Eq. (23)] are well-behaved so long as $\mathcal{W}_s$ is nonzero, or equivalently so long as $\tilde{\omega}_R \neq 0$ and phase velocity $\tilde{\omega}_R/\tilde{k}_y$ is far from electron cyclotron resonance. For a smooth $f_{s0}(v_\perp)$ evaluated at discrete points $v_{\perp,j}$, the integral can be evaluated numerically by first applying adaptive quadrature for the ϕ-integration and applying the trapezoidal rule for integration over the $v_\perp$ direction. If the equilibrium distribution function happens to be Maxwellian, then the magnetized-species susceptibility given by Eq. (23) simplifies to

$$
\begin{aligned}
\chi_s^{\mathrm{mag}}&(\tilde{\omega}, \tilde{k}_y)\big|_{f_{s0}=\text{Maxwellian}} \\
&= \frac{\omega_{ps}^2}{\Omega_s^2} \int_0^{2\pi} \frac{\sin(\theta)}{1 - \exp(2\pi i \mathcal{W}_s)} \\
&\quad \times \exp\left(\tilde{k}_y^2 \tilde{r}_{Ls}^2 [\cos\theta - 1] + i\mathcal{W}_s\theta\right) d\theta,
\end{aligned}
\tag{45}
$$

where $\tilde{r}_{Ls}$ is the species Larmor radius. When $\tilde{k}_y^2 \tilde{r}_{Ls}^2 \gg 1$, the exponential term in Eq. (45) drops off rapidly to zero in the middle of the integration interval. In this case, Taylor expanding $\cos\theta$ term about $\theta = 0$ and $\theta = 2\pi$ facilitates more efficient integration over θ while retaining accuracy.

The integral that appears in the unmagnetized species susceptibility χ_s^{unmag} [see Eq. (25)] is well-behaved so long as $\tilde{\omega}_I$ is finite. In this case, for a discrete $f_s(v_y)$, $\partial f_s/\partial v_y$ can be computed using discrete Fourier transforms and the integral can be evaluated straightforwardly by multiplying the numerator and denominator of the integrand by the complex conjugate of $(\tilde{\omega}/\tilde{k}_y - \tilde{v}_y)$. In the small growth rate limit, i.e., when $\tilde{\omega}_I \ll \tilde{\omega}_R$, the Sokhotskyi-Plemelj formula is applicable and χ_s^{unmag} can be approximated by

$$
\begin{aligned}
\chi_s^{\mathrm{unmag}}(\tilde{\omega}, \tilde{k}_y) \approx \frac{\tilde{\omega}_{pi}^2}{\tilde{k}_y^2} &\left[\text{p.v.} \int_{-\infty}^\infty \frac{1}{\tilde{\omega}_R/\tilde{k}_y - \tilde{v}_y} \frac{\partial \tilde{f}_0}{\partial \tilde{v}_y} d\tilde{v}_y \right. \\
&\left. - i\pi \tilde{f}_0\left(\frac{\tilde{\omega}_R}{\tilde{k}_y}\right) \right]
\end{aligned}
\tag{46}
$$

where p.v. denotes Cauchy principal value, which can be evaluated using the Hilbert transform [24]. For a Maxwellian equilibrium distribution, small-growth-rate approximations are unnecessary, and the unmagnetized-species susceptibility for $\tilde{\omega} \notin \mathbb{R}$ is

$$
\begin{aligned}
\chi_s^{\mathrm{unmag}}\big|_{f_{s0}=\text{Maxwellian}} &= \frac{\tilde{\omega}_{pi}^2}{\tilde{k}_y^2 \tilde{v}_{Ts}^2}\left(1 + i\pi^{1/2}\xi \exp(-\xi^2)\right. \\
&\quad \left. \times [1 + \mathrm{erf}(i\xi)]\right), \\
\xi &= \frac{\tilde{\omega}}{\sqrt{2}\tilde{v}_{Ts}\tilde{k}_y},
\end{aligned}
\tag{47}
$$

where $\tilde{v}_{Ts} = \sqrt{T_s/m_s}$ is the species thermal speed and T_s is the species temperature.

Given the above strategy for evaluating the integrals in $\epsilon(\tilde{\omega}, \tilde{k}_y)$ and provided the growth rate is larger than zero, the dispersion relation can be solved for mixed complex frequency $\tilde{\omega} = \tilde{\omega}_R + i\tilde{\omega}_I$ as a function of wave number using the Nyquist method [53] combined with a bisection algorithm. The Nyquist method facilitates determining whether an unstable root exists in a given region of the $(\tilde{\omega}_R, \tilde{\omega}_I)$ plane and the bisection algorithm enables locating the root(s) to within a tolerance. In practice, the Nyquist method is implemented as follows. For fixed wave number, a closed rectangular contour Γ is chosen in the upper half of the complex $(\tilde{\omega}_R, \tilde{\omega}_I)$ plane. The region enclosed by Γ should contain the unstable root. The choice of contour can be informed by roots obtained from cold-fluid theory. Following Γ counterclockwise in discrete steps, the parametric curve C given by $[\frac{1}{\epsilon_R(\Gamma)}, \frac{1}{\epsilon_I(\Gamma)}]$ is mapped out, where subscripts denote the real and imaginary parts, such that $\epsilon = \epsilon_R + i\epsilon_I$. The integer number of times that C encircles the origin, a.k.a. the winding number, is equal to the number of unstable modes. An automated means of counting the winding number is described in Ref. [53]. The Nyquist method effectively applies the residue theorem to count the number of singularities, i.e., unstable solutions to the dispersion relation, in the region enclosed by Γ. Since the Nyquist method only provides an indication of whether an unstable root exists, it is useful to embed the method in a bisection algorithm so that the contour Γ is iteratively bisected (first in $\tilde{\omega}_I$ then in $\tilde{\omega}_R$) to locate, within a tolerance, the most unstable root. The Nyquist method can be made more efficient by adapting the size of the step taken along Γ based on the angle traversed by the curve C. Likewise, choosing a smaller contour for Γ can speed-up convergence. The Nyquist method is much more computationally efficient for Maxwellian distribution functions than for general distribution functions.

For purely real roots, one can use the bisection method on its own to find solutions between ion cyclotron harmonics. When choosing an interval to bisect, it is important that the interval does not contain cyclotron resonances ($\mathcal{W}_s = 0$), where $\epsilon(\tilde{\omega}, \tilde{k}_y)$ blows up.

Anticipating the need to find roots repeatedly for evolving distribution functions, one can take advantage of known solutions. For example, if $\tilde{\omega}^\mathcal{M}(\tilde{k}_y)$ is the solution to the dispersion relation obtained using the Nyquist-bisection method for a Maxwellian equilibrium distribution function, then a minimum-finding optimization algorithm (e.g., Levenberg-Marquardt) can be applied to find the zeros of $|\epsilon|$ for a slightly different distribution function using $\tilde{\omega}^\mathcal{M}$ as the initial guess.

Solutions to the dispersion relation can also be approximated by assuming $\tilde{\omega}_I \ll \tilde{\omega}_R$ and Taylor expanding $\epsilon(\tilde{\omega}, \tilde{k}_y)$ about $\tilde{\omega} = \tilde{\omega}_R$ in small parameter $\tilde{\omega}_I$ [54]. Retaining terms that are first order in $\tilde{\omega}_I$ and assuming that ϵ_I is $\mathcal{O}(\tilde{\omega}_I^2)$ or smaller, the real frequency can then be obtained by solving $\epsilon_R(\tilde{\omega}_R, \tilde{k}_y) = 0$ for fixed wave number, while the imaginary part of frequency is obtained from

$$
\tilde{\omega}_I = -\frac{\epsilon_I(\tilde{\omega}_R)}{\frac{\partial \epsilon_R}{\partial \tilde{\omega}_R}\big|_{\tilde{\omega}=\tilde{\omega}_R}}.
\tag{48}
$$

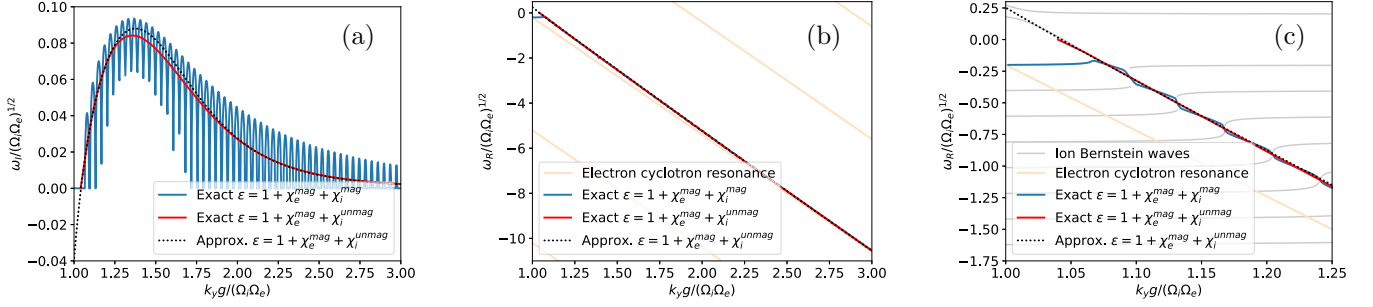As will be discussed, the assumptions necessary for this approximation to be accurate are not always met.

FIG. 2. Growth rate ω_I in plot (a) and frequency ω_R in plots (b) and (c) as a function of wave number for acceleration-driven LHDI, assuming ion and electron equilibrium distribution functions are Maxwellian. The dispersion relation is evaluated for dimensionless parameters $m_i/m_e = 25$, $\Omega_e/\omega_{pe} = 0.5$, $T_i/T_e = 1$, $V_d/v_{Ti} = 3.12$, $\beta = 2.5 \times 10^{-3}$. Plot (c) is a zoomed-in version of plot (b), and shows a smaller range of wave numbers and frequencies to illustrate how unstable mode interconnects with ion Bernstein waves (gray lines). Solutions are shown to three different forms of the dispersion relation: one in which both ions and electrons are magnetized [Eq. (22)], one where electrons are magnetized and ions are unmagnetized [Eq. (26)], and an approximate dispersion relation based on Taylor expansion for the case where ions are unmagnetized [see Eq. (48)]. In all cases, the threshold for the instability is $k_y g/|\Omega_i \Omega_e| \gtrsim 1$ and real frequency solutions fall near electron cyclotron resonances. Treating ions as magnetized introduces fine-scale structure to the dispersion relation. The approximate dispersion relation is inaccurate in the vicinity of $k_y g/(\Omega_i \Omega_e) \approx 1$.

Figure 2 shows solutions to three different forms of the dispersion relation: one in which electrons and ions are both magnetized, as defined in Eq. (22); one in which ions are unmagnetized, as defined in Eq. (26); and one in which ions are unmagnetized and the Taylor-series-based approximation is applied such that $\epsilon(\tilde{\omega}_R, \tilde{k}_y) = 0$ is used to solve for $\tilde{\omega}_R$ and Eq. (48) is invoked to solve for growth rate. The dispersion relations are solved assuming ion and electron distribution functions are Maxwellian for parameters $m_i/m_e = 25$, $\Omega_e/\omega_{pe} = 0.5$, $T_i/T_e = 1$, $V_d/v_{Ti} = 3.12$, where $V_d = u_{yi} - u_{ye} = (g/\Omega_i - g/\Omega_e)$ is the relative drift velocity. Plasma beta, the ratio of thermal pressure to magnetic pressure, is set to $\beta = 2.5 \times 10^{-3}$. The instability also exists at realistic mass ratios, as demonstrated in Fig. 3, which shows the growth rate as a function of wave number for the parameter case $m_i/m_e = 1836$, $\Omega_e/\omega_{pe} = 0.107$, $T_i/T_e = 1$, $V_d/v_{Ti} = 3.00$, $\beta = 2.5 \times 10^{-3}$—again assuming distribution functions are Maxwellian. All forms of the dispersion relation, independent of parameters, have an instability threshold of $\tilde{k}_y \approx k_y r_{Le}(\frac{V_d}{v_{Ti}})(\frac{m_e}{m_i})^{1/2}(\frac{T_i}{T_e})^{1/2} \gtrsim 1$. This property is consistent with the cold-fluid dispersion relation given by Eq. (B3) in Appendix B. All forms of the dispersion relation also have peak growth rates at wave numbers that roughly coincide—see Figs. 2(a) and 3. The approximate form of the unmagnetized-ion dispersion relation is, as expected, not accurate at wave numbers for which $\tilde{\omega}_I = \mathcal{O}(\tilde{\omega}_R)$ as evidenced by negative growth rate solutions in Fig. 2—here the solution to the approximate dispersion relation does not satisfy $\epsilon(\tilde{\omega}, \tilde{k}_y) = 0$ for $\tilde{k}_y$ values near unity. The accuracy of the Taylor series approximation improves when mass ratio is increased. The magnetized-ion dispersion relation exhibits fine-scale structure that is related to the presence of the ion gyroradius scale length. In particular, the structure becomes finer as m_i/m_e or T_e/T_i increases. The structure is observed both in the growth rate $\tilde{\omega}_I$, as well as in the real frequency $\tilde{\omega}_R(\tilde{k}_y)$—see Figs. 2(a) and 2(c). As evidenced in Fig. 2(c), when ions are treated as magnetized, mixed-complex frequencies branch with ion Bernstein waves. The exact form of the unmagnetized-ion

dispersion relation does not include ion Bernstein waves, and hence does not support purely real roots. Overall growth rates increase with V_d/v_{Ti} and with ω_{pe}/Ω_e, i.e., when more drift energy is available to drive the instability.
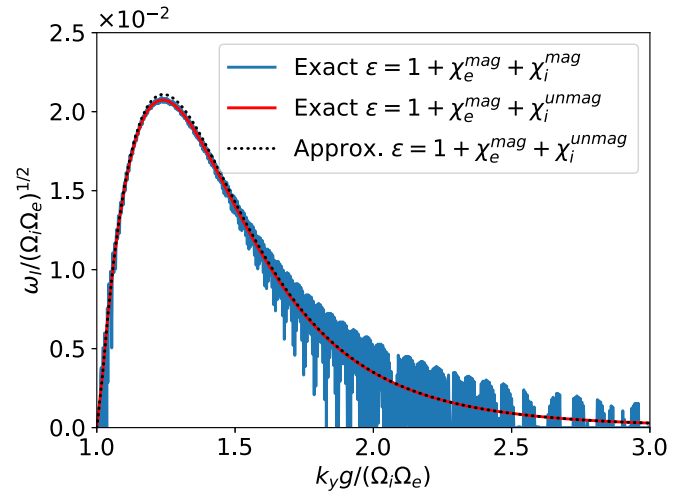

FIG. 3. Growth rate as a function of wave number obtained by solving the acceleration-driven LHDI dispersion relation for realistic mass ratio with parameters $m_i/m_e = 1836$, $\Omega_e/\omega_{pe} = 0.107$, $T_i/T_e = 1$, $V_d/v_{Ti} = 3.00$, $\beta = 2.5 \times 10^{-3}$. Ion and electron distribution functions are taken to be Maxwellian. Solutions are shown to three different forms of the dispersion relation: one in which both ions and electrons are magnetized [Eq. (22)], one where electrons are magnetized and ions are unmagnetized [Eq. (26)], and an approximate dispersion relation based on Taylor expansion for the case where ions are unmagnetized [see Eq. (48)]. With increased mass ratio, the magnetized-ion dispersion relation solution exhibits finer structure (which is not fully resolved here) and the solution to the approximate dispersion relation approaches the solution to the exact dispersion relation. For this wave-number interval, real frequencies for the instability (not shown) fall in the range $\omega_R/(\Omega_i \Omega_e)^{1/2} \in [-82, 0]$.

The main distinctive features are that magnetized-ion dispersion relation exhibits fine-scale structure, that—as expected—the approximate dispersion relation is inaccurate in parameter regions where $\tilde{\omega}_I \approx \tilde{\omega}_R$, and that all dispersion relations have an instability threshold of $\tilde{k}_y \gtrsim 1$.

B. Solving quasilinear diffusion model

Given initial conditions and boundary conditions, the nonlinear coupled diffusion equation system in Sec. IV [defined by Eq. (33) for magnetized electrons, Eq. (33) or Eq. (38) for ions, and Eq. (36) for the electric-field energy spectrum] can be discretized and solved numerically and self-consistently for f_{i0}, f_{e0}, and $\mathcal{E}_k$ as a function of time. Here a second-order Crank-Nicolson method with a second-order finite-volume discretization is used.

Averaging Eq. (33) over a velocity-space cell volume, denoted by cell-center index j with cell edges at indices $j \pm \frac{1}{2}$, facilitates recasting the magnetized-species diffusion equation into weak form, such that the time derivative of the cell-average distribution function $\langle f \rangle_j$ is

$$\frac{\partial}{\partial t}\langle f \rangle_j = \left[v_\perp D_v \frac{\partial f}{\partial v_\perp} \right]_{j-\frac{1}{2}}^{j+\frac{1}{2}}, \tag{49}$$

where in the interest of clarity we have omitted subscript s denoting species and superscript mag denoting magnetized-species diffusion coefficient, which is defined in Eq. (34). The advantage of the weak form is that it admits solutions that can have local discontinuities.

A second-order accurate finite-difference Crank-Nicolson method is used for time discretization. Letting ℓ be the time index, then $\langle f \rangle^{\ell+1}$ is related to $\langle f \rangle^\ell$ through

$$\frac{1}{\Delta t}\left(\langle f \rangle_j^{\ell+1} - \langle f \rangle_j^\ell \right) = \frac{1}{2}\left(\left[v_\perp D_v \frac{\partial f}{\partial v_\perp} \right]_{j-\frac{1}{2}}^{j+\frac{1}{2}} \right)^{\ell+1}$$
$$+ \frac{1}{2}\left(\left[v_\perp D_v \frac{\partial f}{\partial v_\perp} \right]_{j-\frac{1}{2}}^{j+\frac{1}{2}} \right)^\ell. \tag{50}$$

To approximate the unknown nonlinear velocity-space diffusion coefficient $D_v^{\ell+1}$, we use a Taylor series expansion and finite differences, such that $D_v^{\ell+1} = D_v^\ell + \frac{dD_v^\ell}{dt}\Delta t = D_v^\ell + \frac{1}{2}(D_v^\ell - D_v^{\ell-2})$. Equation (50) can be recast as a matrix time-update equation for $\langle f \rangle_j^\ell$, in which each row j corresponds to a different velocity-space cell:

$$\left(\frac{1}{\Delta t} - \frac{1}{2}\left[v_\perp D_v^{\ell+1} \frac{\partial}{\partial v_\perp} \right]_{j-\frac{1}{2}}^{j+\frac{1}{2}} \right)\langle f \rangle_j^{\ell+1}$$
$$= \left(\frac{1}{\Delta t} + \frac{1}{2}\left[v_\perp D_v^\ell \frac{\partial}{\partial v_\perp} \right]_{j-\frac{1}{2}}^{j+\frac{1}{2}} \right)\langle f \rangle_j^\ell, \tag{51}$$

where Δt is the time-step size (see Appendix C) and derivatives $\partial f/\partial v_\perp$ are evaluated using second-order finite-difference stencils, which results in a second-order finite-volume velocity-space spatial discretization. Equation (51) can be solved for $\langle f \rangle_j^{\ell+1}$ using a linear algebra solver. The unmagnetized-species diffusion equation of Eq. (38) can be discretized in the same fashion.

Since diffusion is an initial-boundary value problem, boundary conditions are needed for the distribution function f_s. To allow for diffusion everywhere in the velocity-space domain and to ensure net conservation of mass, we set homogeneous Neumann boundary conditions, such that velocity gradients are zero at all velocity boundaries. These boundary conditions are implemented by modifying the boundary cell stencils in Eq. (51).

The spectral electric-field energy density, $\mathcal{E}_k$, is advanced forward in time in accordance with Eq. (36), such that

$$\mathcal{E}_k(t) = \mathcal{E}_{k0} \exp\left(2\int_0^t \omega_I(k_y, t')dt' \right), \tag{52}$$

where $\mathcal{E}_{k0}$ is the initial $t = 0$ value and the cumulative time integral is evaluated using a second-order trapezoidal rule.

Initial conditions are set as follows. The initial species distribution functions are chosen to be Maxwellian, centered at the origin, with normalization $\int f_s d\boldsymbol{v} = 1$. The initial spectral electric-field energy density $\mathcal{E}_{k0}$ is set to a constant value independent of wave number so that the ratio of electric-field energy [see Eq. (37)] to thermal energy is $\mathcal{E}/[n(T_i + T_e)] \approx 1 \times 10^{-9}$ at initial time, i.e., a very small value as is necessary for quasilinear theory to be applicable. Alternatively, $\mathcal{E}_{k0}$ can be set to be the maximum of a near-zero value and a scalar multiple of the growth rate $\omega_I(k_y)$ at initial time, as done in
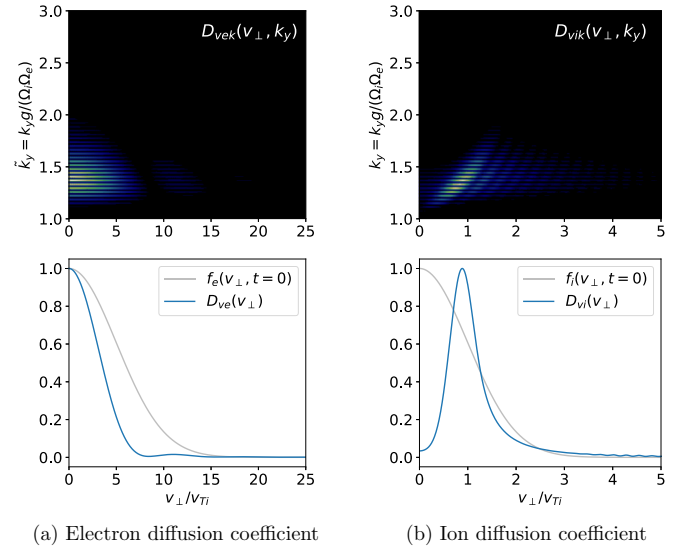

(a) Electron diffusion coefficient

(b) Ion diffusion coefficient

FIG. 4. The wave-number- and velocity-dependent structure of $D_{vsk}^{\mathrm{mag}}(v_\perp, k_y)$ (top), the integrand used to evaluate the quasilinear theory velocity-space diffusion coefficient $D_{vs}^{\mathrm{mag}}(v_\perp)$ in Eq. (34) for magnetized electrons (left) and magnetized ions (right). The resulting species diffusion coefficient (electrons bottom left; ions bottom right), obtained by integrating D_{vsk}^{mag} over wave number, is normalized to the maximum value, and is plotted alongside the initial species distribution function, which here is also normalized to its peak value. The diffusion coefficient indicates which velocity-space portion of the distribution function is most affected by the LHDI. Because of the wave-number dependence of $\mathcal{E}_k$ and ω_I, both of which appear in the integral expression for the diffusion coefficient in Eq. (34), wave numbers near peak growth rate strongly influence the velocity-space structure of the diffusion coefficient. Here D_{vsk}^{mag} is evaluated after a few instability growth times.

Ref. [24] in exploration of the bump-on-tail instability. Both initializations of $\mathcal{E}_{k0}$ after a time-step result in a $\mathcal{E}_k$ spectrum that is largely determined by the growth rate spectrum. Including modes whose growth rates are initially zero allows for the possibility of those modes developing finite growth rates later in time.

In principle, the wave-number domain and the velocity-space domain are infinite in the quasilinear model. In practice, to obtain discrete solutions, both domains have to be truncated. We consider the truncated wave-number domain $k_y g/(\Omega_i \Omega_e) \in [1, 3]$, which is chosen because for parameter cases explored here (which are by no means exhaustive), modes outside this wave-number range appear to have a negligible effect on the distribution functions. The velocity domain is defined to be $v_{\perp s}/v_{Ts} \in [0, 5]$ for magnetized species and $v_y/v_{Ti} \in [-5, 5]$ for unmagnetized ions. For the two-species plasma under consideration, ions are treated either as magnetized or unmagnetized (not both). For magnetized species,

1000 wave numbers are used to resolve the detailed structure of the dispersion relation. For unmagnetized species, 392 wave numbers are used. Note that if an insufficient number of wave numbers are used, then the ion diffusion coefficient can become discontinuous in time and/or in velocity space. Wave numbers need not be uniformly spaced. Figure 4 shows for a given $\mathcal{E}_{k0}$ how the diffusion coefficient depends on wave number and velocity coordinate. In the magnetized-ion quasilinear model, 288 points are used to discretize velocity space. In the unmagnetized-ion model 864 velocity grid points are used. The exact number of discrete points in wave number and velocity space is informed by computational cost considerations, available parallelization, and the structure of the diffusion coefficient integrand D_{vsk} [see Eqs. (34) and (39) and Fig. 4]. The parameter case considered is described after Eq. (48) in Sec. V A. The algorithm for the updating cell-average $\langle f_s \rangle_j$ and $\mathcal{E}_k$ is given below.

ALGORITHM 1. Solving quasilinear diffusion equation system.

---

discretize each species' velocity domain;

discretize wavenumber domain;

initialize distribution functions and spectral electric field energy density;

solve dispersion relation using Nyquist method and save time t=0 frequency solution ω;

for *each time step* **do**

    for *each wavenumber* **do**

        solve dispersion relation for mixed-complex frequency $\omega = \omega_R + i\omega_I$ using Levenberg-Marquardt

          algorithm with previous time step frequency as initial guess;

        evaluate $\mathcal{E}_k(t)$ using imaginary part of frequency ω_I;

        for *each species* **do**

            evaluate integrand D_{vsk} of species diffusion coefficient using frequency ω;

        end

    end

    for *each species* **do**

        Evaluate diffusion coefficient D_{vs} by integrating D_{vsk} over wavenumber;

        Update distribution function f_s using Crank-Nicolson time advance;

    end

    Adjust time step size Δt;

end

As discussed in Sec. V A, using the Levenberg-Marquardt optimization algorithm for finding roots of the dispersion relation [either Eq. (22) or Eq. (26)] increases solution speed. The computational efficiency of the algorithm is substantially improved by parallelizing the wave number for-loop. Further gains in efficiency are achieved by adapting time-step size so that the relative changes $(\mathcal{E}^{\ell+1} - \mathcal{E}^\ell)/\mathcal{E}^\ell$ and $\max_j(|\langle f_s \rangle_j^{\ell+1} - \langle f_s \rangle_j^\ell|/\langle f_s \rangle_j^\ell)$ are less than about 2%. Dispersion relations in Eqs. (22) and (26) provide a useful check on the quasilinear solver. For all numerical solutions to the quasilinear theory governing equations that are presented here, it has been verified that for finite ω_I (i.e., finite diffusion), the equality

$\epsilon(\omega_R + i\omega_I, k_y) = 0$ holds to a tolerance of about $\pm 5 \times 10^{-6}$ for all time—a very small value compared to the susceptibilities, which are of order unity. To ensure this tolerance is met, growth rates in the unmagnetized-ion quasilinear description have to be zeroed out whenever the unmagnetized-ion approximation is violated, i.e., when $\omega_R/\Omega_i < 1$. Furthermore, it was found that using the commonly applied Taylor series approximations to solve a given dispersion relation [see Eq. (48) and surrounding text] could lead to $\epsilon(\omega_R + i\omega_I, k_y)$ being far from zero—particularly as the instability transitions from linear to nonlinear regime. This can potentially explain some of the discrepancies seen between quasilinear calculations and Vlasov

simulations in Ref. [24], where a Taylor series approximation was employed. As such, Taylor series approximations of the form in Eq. (48) are not employed here in numerical solutions to the quasilinear governing equations.

VI. VLASOV SOLVER, INITIAL CONDITIONS, BOUNDARY CONDITIONS, AND SETUP

Vlasov simulations are carried out using the parallel fourth-order accurate (in space and time) conservative finite-volume *Vlasov Continuum Kinetics* (VCK) code [38,55]. The code has been benchmarked [38], has been demonstrated to have robust convergence properties [38,55], and has been successfully applied in investigations of the Dory-Guest-Harris instability [38], dynamics of axisymmetric plasmas [55], nonuniform equilibria [36], gyromotion-modulated Kelvin-Helmholtz instabilities [12,56], and gradient-driven lower hybrid drift instabilities [56]. When it comes to cross-comparisons with quasilinear theory, an important strength of continuum kinetic solvers like VCK is that they provide smooth differentiable solutions. This advantage has been demonstrated previously in quasilinear and nonlinear simulation studies of the bump-on-tail instability [24].

For the purposes of modeling the acceleration-driven LHDI, VCK is applied to solve the Vlasov-Poisson equation system in Eqs. (1) and (2) in 3D (y, v_x, v_y) phase space with resolution $N_y \times N_{v_x} \times N_{v_y} = 1152 \times 512 \times 512$. At initial time, ion and electron distribution functions are set to be drifting Maxwellians, such that

$$f_s(y, v_x, v_y)|_{t=0} = \frac{m_s}{2\pi T_s} \exp\left(-\frac{m_s\left(v_x^2 + \left[v_y - \frac{g}{\Omega_s}\right]^2\right)}{2T_s}\right),$$
(53)

where temperature $T_s = m_s v_{Ts}^2$. The spatial domain is periodic and of length $L_y = 20\pi/k_{max}$, where k_{max} is the fastest growing mode according to the dispersion relation in Eq. (22). In effect, the domain is ten times longer than the wavelength of the fastest growing mode. The velocity domain is set to span 18 thermal speeds in each velocity direction and to be centered at the centroid of each velocity distribution function, such that the v_x velocity extent is $v_{xs}/v_{Ts} \in [-9, 9]$ for each species and the v_y velocity extent is $v_{yi}/v_{Ti} \in [-6, 12]$ for ions and $v_{ye}/v_{Te} \in [-9.024, 8.976]$ for electrons. Zero flux boundary conditions are applied at velocity boundaries to ensure conservation of the distribution function.

The equilibrium is perturbed with a sinc function perturbation by multiplying f_s by $1 + \alpha \ \mathrm{sinc}(h[y - L_y/2])$, with the sinc function defined as $\mathrm{sinc}(x) = \frac{\sin(x)}{x}$ and amplitude $\alpha = 8 \times 10^{-5}$. The parameter h is chosen to ensure the perturbation is periodic in the domain of length L_y and so that modes in the approximate range $k_y \in [-2k_{max}, 2k_{max}]$ are perturbed. In effect $h \approx 2k_{max}$. The sinc function is a smooth approximation to a delta function and is chosen because it has a broad continuous wave-number spectrum that excites all modes with the same amplitude. To assess sensitivity of nonlinear solutions to different types of perturbations in the context of the Vlasov-Poisson solver, we also consider a sum-of-sines perturbation with 13 wavelengths. Unless

otherwise specified, the results presented will be from the Vlasov simulation that uses a sinc function perturbation. While we present results exclusively from $1152 \times 512 \times 512$ resolution Vlasov simulations, to gauge sensitivity to resolution, we have performed simulations with a lower velocity-space resolution of $N_y \times N_{v_x} \times N_{v_y} = 1152 \times 256 \times 256$ and found that the deviations between high-resolution and low-resolution results are small and are on par with the deviation between sum-of-sines perturbation and sinc-function perturbation results shown in Fig. 5.

VII. COMPARING QUASILINEAR MODEL AGAINST VLASOV SIMULATIONS FOR THE ACCELERATION-DRIVEN LHDI

The nonlinear acceleration-driven LHDI is explored using the Vlasov-Poisson solver and the quasilinear model solver for the parameter case $m_i/m_e = 25$, $\Omega_e/\omega_{pe} = 0.5$, $T_i/T_e = 1$, $V_d/v_{Ti} = 3.12$, which is first discussed in Sec. V A. To keep a clear distinction, we will refer to quasilinear model numerical solutions as "calculations" and Vlasov-Poisson numerical solutions as "simulations" and cross-compare features of the evolving plasma state within the two models. An artificial mass ratio of $m_i/m_e = 25$ is used to lower the computational cost of the Vlasov-Poisson solver and make simulations tractable. See Appendix C for how mass ratio affects the compute time of Vlasov and quasilinear model solvers.

A. Electric-field energy

Evolution of electric-field energy density as a function of time provides one indicator of the linear-to-nonlinear transition of the acceleration-driven LHDI. Electric-field energy is also an important measure of quasilinear theory's predictive capability because it determines the magnitude of diffusion and transport terms. Figure 5 shows electric-field energy evolution from a magnetized-ion quasilinear calculation, unmagnetized-ion quasilinear calculation, and Vlasov simulations using different initializations. Maximum growth rates according to magnetized-ion [Eq. (22)] and unmagnetized-ion [Eq. (26)] linear theory for acceleration-driven LHDI are also shown for reference.

In Vlasov simulations, the electric-field energy initially grows exponentially in time at a growth rate that is consistent with unmagnetized-ion linear theory. As with all instabilities, nonlinear effects eventually come into play, exponential growth stops, and electric-field energy oscillates about a nearly constant saturated value. Figure 5 shows that using a sinc-function perturbation, which has a piecewise-uniform wave-number spectrum, results in a slightly larger saturated value of electric-field energy than when using a sum-of-sines perturbation. Overall, however, Vlasov simulation results are not particularly sensitive to the exact form or amplitude of the initial perturbation, so long as the perturbation amplitude is small.

In quasilinear calculations, the electric-field energy density transitions from exponential growth at a rate predicted by unmagnetized-ion linear theory to a much smaller growth rate, but never saturates, as shown in Fig. 5. The lack of saturation
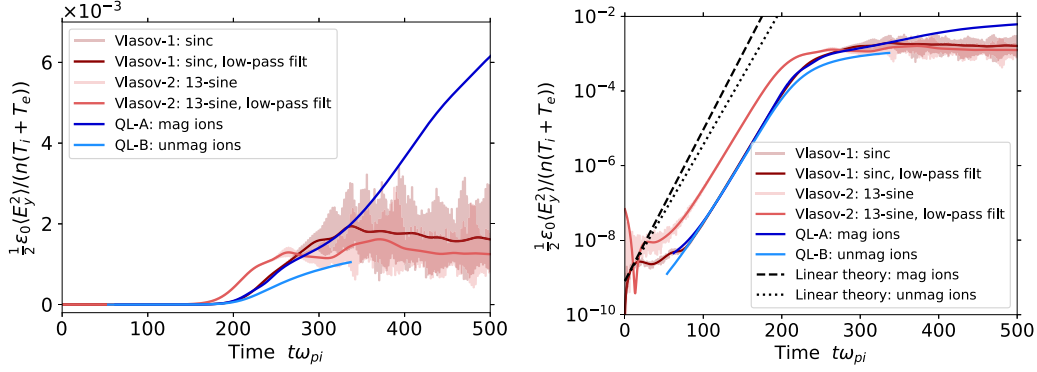
FIG. 5. Evolution of electric-field energy density relative to initial thermal energy density, $n(T_i + T_e)$, in Vlasov simulation with sinc function perturbation (Vlasov-1), Vlasov simulation with a sum-of-sines perturbation (Vlasov-2), quasilinear calculation with magnetized ions (QL-A), and quasilinear calculation with unmagnetized ions (QL-B). Quasilinear calculation time traces are shifted in time to overlay with the linear stage of the Vlasov-1 time trace. This time offset is equivalent to using a different perturbation amplitude in the linear phase. Vlasov simulation low-pass filtered traces are shown in addition to the raw data. The evolution is shown on a linear scale (left) and a log scale (right). The linear theory growth rates for the fastest growing mode, according to magnetized-ion dispersion relation and unmagnetized-ion dispersion relation, are shown for reference. Vlasov simulations exhibit a clear transition from linear-theory-predicted exponential growth to a saturated state, wherein the electric-field energy density oscillates around a nearly constant value. E-field energy density in quasilinear calculations also exhibits a transition from linear-theory-predicted exponential growth to a much smaller growth rate, but never saturates.

is due to the fact that an LHDI driver (i.e., acceleration) is always present and there is no damping mechanism (e.g., no Landau damping) for the waves in the quasilinear description, which means that growth rates remain nonnegative for all time. In principle, growth rates can become zero when temperature reaches a sufficiently high value such that a stable configuration is reached. Magnetized-ion and unmagnetized-ion quasilinear calculations yield different time histories, such that magnetized-ion treatment results in higher electric-field energy density at the linear-to-nonlinear transition. Vlasov simulation nonlinear time history appears to fall between the magnetized-ion and unmagnetized-ion quasilinear calculations.

The choice of initialized $\mathcal{E}_{k0}$ [see Eq. (52)] in quasilinear calculations can modify the electric-field energy density during the nonlinear stage, but as with Vlasov simulations, the results are not particularly sensitive to the exact form of initial condition. While $\mathcal{E}_k$ is real-valued and only depends on growth rate, one can reintroduce phase information by evolving a mixed-complex spectral electric field, according to

$$\hat{E}_{1k} = \hat{E}_{1k0} \exp\left(-i \int_0^t (\omega_R + i\omega_I)dt'\right) \text{ for } k_y \in (-\infty, \infty) \tag{54}$$

and with various choices for mixed complex $\hat{E}_{1k0}$ that satisfy Eq. (30) one can verify that the resulting electric-field energy evolution [see Eqs. (35) and (37) for the relationship between these variables] is likewise not particularly sensitive to initial conditions, including phase information. For all initializations of $\mathcal{E}_{k0}$ and $\hat{E}_{1k0}$ that we have tested, including different wave-number dependence and different magnitudes satisfying $\mathcal{E}/[n(T_i + T_e)] \ll 1$, saturated state conditions fall within about 20% of each others.

As shown in Fig. 5, depending on what metric is used to define "saturation" in the quasilinear calculations, the quasilinear predictions of electric-field energy density can be

within a factor of two of Vlasov simulation results. This points to a need for a metric that can be used to identify at which point in instability evolution is quasilinear theory no longer applicable. We will return to this topic later in the paper.

B. Electric-field spectrum and growth rates

Different wave-number modes contribute to the net electric-field energy, and the overall spectrum ultimately dictates anomalous transport. The validity of the quasilinear description thus, in part, depends on its ability to capture the relative contributions of different modes (even if the theory does not capture damping). These relative contributions can be measured by growth rate as a function of wave number and time. While growth rate is explicitly solved for in the quasilinear model, Vlasov simulations growth rates can be obtained by taking the discrete spatial Fourier transform of $E_y(y, t)$ to get $\hat{E}_k(k_y, t)$, multiplying by the complex conjugate to get $|\hat{E}_k|^2$, applying a low-pass filter in time to smooth out high-frequency variations, evaluating the time derivative of the log of the result, and dividing by two. Fig. 6 compares growth rates from a sinc-perturbation Vlasov simulation and quasilinear calculations. The evolution of growth rates is subject to certain inherent features of the given model. The fine scale structures in $\omega_I(k_y)$ from magnetized-ion quasilinear calculation reflects the initial dispersion relation structure shown in Fig. 2. Apart from this inherent difference, the evolution of growth rate in the magnetized-ion and unmagnetized-ion calculations is also markedly different at low wave numbers because unmagnetized-ion quasilinear treatment is not valid when ω_R/Ω_i is of order unity. This leads to disproportionately high growth rates at low wave numbers next to zero growth rates (where growth rates are explicitly zeroed out for not satisfying the dispersion relation) in the unmagnetized-ion quasilinear treatment. The Vlasov simulation has lower wave-number resolution than quasilinear calculations since it only captures wave numbers that are integer multiples of $2\pi/L_y$.
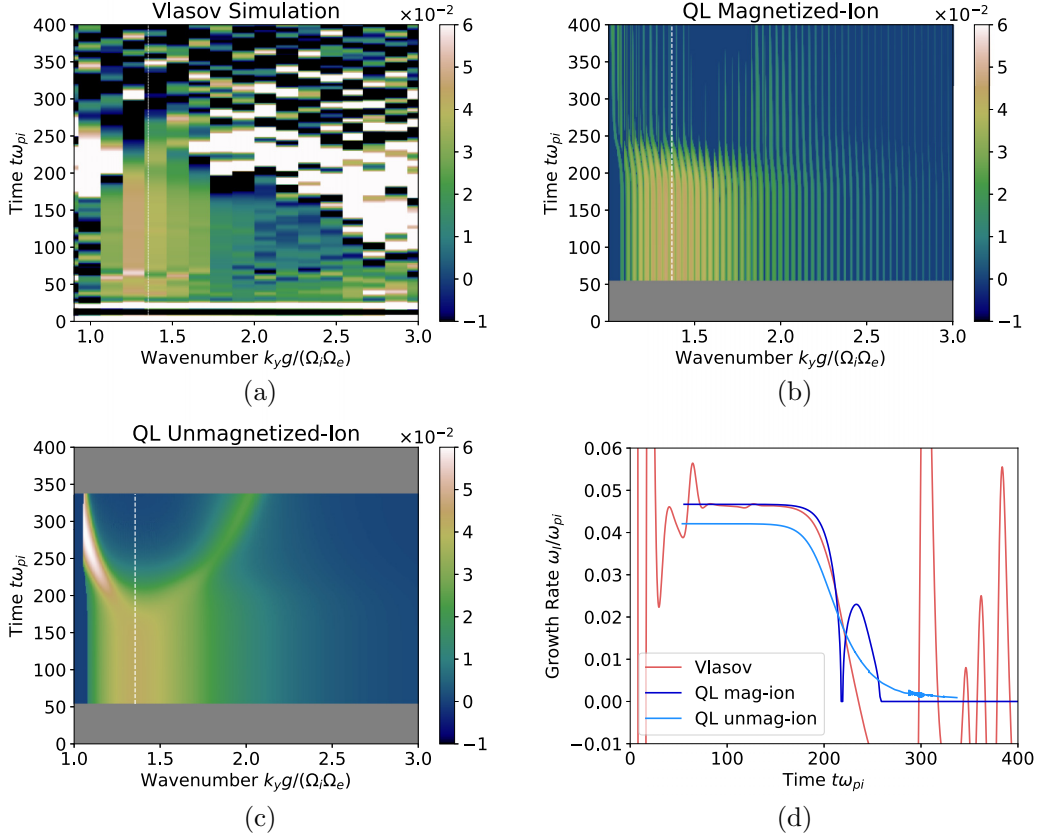
FIG. 6. Growth rate $\omega_I/\omega_{\rm pi}$ as a function of wave number and time from (a) Vlasov simulation with sinc perturbation, (b) quasilinear calculation with magnetized ions, and (c) quasilinear calculation with unmagnetized ions. Dashed vertical white lines denote the wave number of the fastest-growing mode at initial time. The temporal evolution of the growth rate for this initially fastest-growing mode is shown for all three cases in panel (d). All contours are capped at 6×10^{-2} and are floored at -1×10^{-2}. Vlasov simulations only capture wave numbers that are integer multiples of $2\pi/L_y$ and thereby are not as resolved in wave-number space as the quasilinear calculations. While quasilinear growth rates are nonnegative, Vlasov simulation growth rates can be negative, indicating the presence of damping. Vlasov simulation growth rates have a much larger range than growth rates from the quasilinear calculations. Growth rates in the unmagnetized-ion quasilinear calculation are zeroed out whenever the unmagnetized-ion approximation is violated, i.e., when $\omega_R/\Omega_i < 1$. Gray regions signify no data, e.g., due to time shift of quasilinear calculations to match with Vlasov simulation. Quasilinear calculations and the Vlasov simulation both show that the growth rate of the initially fastest-growing mode decreases in time, and that neighboring modes—including those that were initially stable—take on larger growth rates and/or become more important.

While quasilinear calculations do not reflect the exact growth rate values seen in the Vlasov simulation, they do capture aspects of nonlinear growth rate evolution. Specifically, quasilinear calculations successfully capture the trend of initially fastest-growing modes diminishing in importance, and initially smaller-growth-rate modes (including those at lower wave numbers that are initially stable) becoming more important. This trend is consistent with ion distribution function deformation—as the distribution function flattens at phase velocities associated with high growth rates, neighboring velocity-space regions develop larger gradients that lead to larger growth rates. The relationship between $\omega_I(k_y)$ and the electron distribution function structure is less apparent. Quasilinear calculations are characterized by nonnegative growth rates for all time, whereas in Vlasov simulations, after the linear regime, mode damping (negative growth rates) occurs intermittently with mode growth (positive growth rates). Negative growth rates in Vlasov simulations confirm that a damping mechanism is present that is not captured by the quasilinear description. Interestingly, the Vlasov simulation

growth rates evolution in Fig. 6(a) is not indicative of strong mode-mode coupling, which suggests that quasilinear theory's neglect of wave-wave interactions may be justified for the parameter case considered.

C. Distribution function evolution

Another important measure of quasilinear theory's applicability is the degree to which velocity-space diffusion accurately captures the nonlinear evolution of the spatially averaged ion and electron distribution functions. Here we examine the structure of the time-evolving distribution functions and the associated diffusion coefficient in the magnetized-ion quasilinear calculation and in the sinc-perturbation Vlasov simulation.

The time-dependent velocity space structure of the ion distribution function and the electron distribution function from the Vlasov simulation is shown in Figs. 7 and 8, respectively. The distribution functions are plotted during the time interval when the acceleration-driven LHDI transitions from linear to
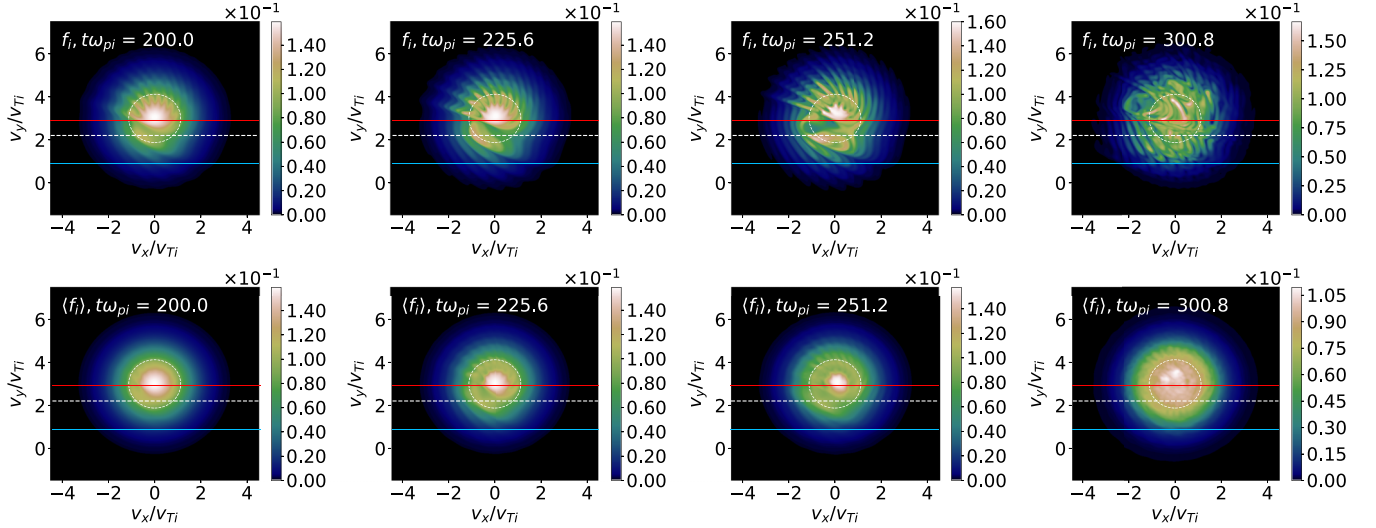
FIG. 7. The ion distribution function at different snapshots in time in the Vlasov simulation. The top row shows the ion distribution function at a fixed y location. Overplotted is the phase velocity of the fastest growing mode (horizontal white dashed line), the minimum phase velocity captured in quasilinear calculation (blue line), and the maximum phase velocity captured in the quasilinear calculation (red line). A fixed unperturbed magnetized particle trajectory is denoted by a white dashed circle. The second row shows the spatially averaged Vlasov simulation ion distribution function, overplotted with the same phase velocity reference lines. These results show that up to a point, the Vlasov simulation spatially averaged ion distribution function diffuses radially outward in velocity space. Although the spatially averaged ion distribution function is not axisymmetric, the minimal azimuthal variation suggests that ion distribution function evolution can—to some degree—be represented as a function of a single $v_\perp$ velocity coordinate, as done in the magnetized-ion quasilinear model.

nonlinear regime, i.e., when distribution function deformation becomes significant. The top row of Fig. 7 shows contour plots of the ion distribution function $f_i(y, v_x, v_y)$ at a fixed y position, and the bottom row in Fig. 7 shows the spatially averaged ion distribution function, $\langle f_i \rangle$. Analogously, Fig. 8 shows the Vlasov simulation evolution of the electron distribution function, with $f_e(y, v_x, v_y)$ at a fixed y location in the top row and the spatially averaged electron distribution

function, $\langle f_e \rangle$ in the bottom row. Figs. 7 and 8 also show a fixed unperturbed magnetized particle trajectory (denoted by a white circle) and the phase velocity $v_{ph} = \omega_R/k$ associated with the fastest growing LHDI mode at initial time (denoted by the horizontal white line) for the parameter case modeled. Red and blue lines denote the maximum and minimum phase velocities within which the LHDI is active for the range of wave numbers under consideration in the quasilinear
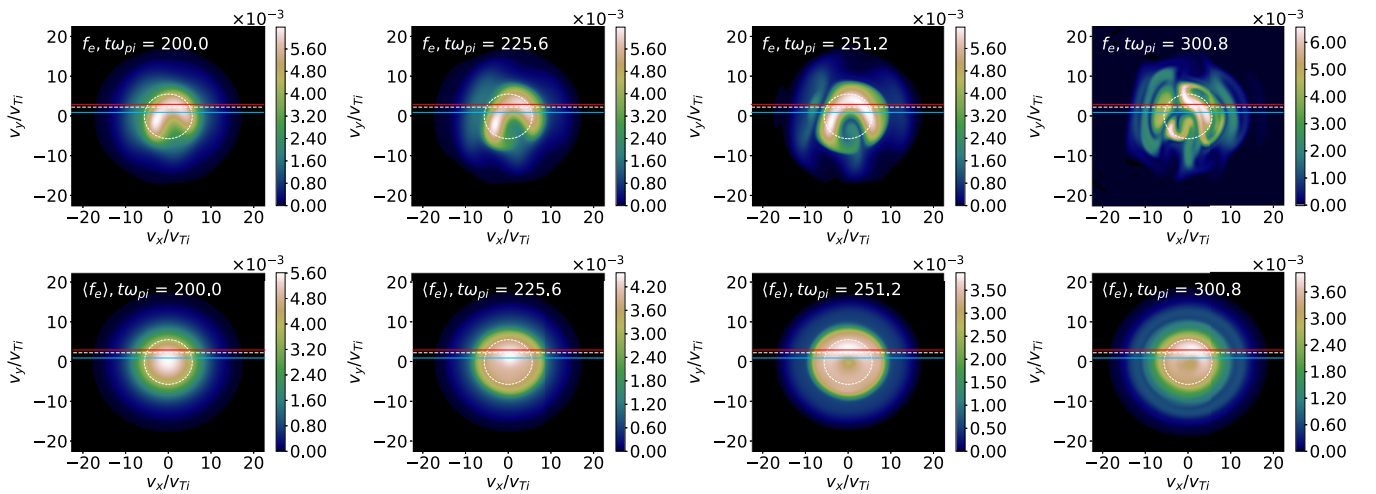

FIG. 8. The electron distribution function at different snapshots in time in the Vlasov simulation. Top row shows the electron distribution function at a fixed y location. Overplotted is the phase velocity of the fastest growing mode (horizontal white dashed line), the minimum phase velocity captured in quasilinear calculation (blue line), and the maximum phase velocity captured in the quasilinear calculation (red line). A fixed unperturbed magnetized particle trajectory is denoted by a white dashed circle. Bottom row shows the spatially averaged Vlasov simulation electron distribution function, overplotted with the same phase velocity reference lines. These results show that up to a point, the Vlasov simulation spatially averaged electron distribution function diffuses radially outward in velocity space and that it can be accurately represented as a function of a single $v_\perp$ velocity coordinate, as done in the quasilinear model description.

calculation. When plotted at a fixed y position at fixed time, the Vlasov-simulation ion distribution function $f_i(v_x, v_y)$ (Fig. 7, first row) and electron distribution function $f_e(v_x, v_y)$ (Fig. 8, first row) both exhibit complex fine-scale structures. Once spatially averaged, however, azimuthal variations are largely absent—as shown in the second row of Figs. 7 and 8. The spatially averaged electron distribution function, in particular, appears to be nearly axisymmetric. Negligible azimuthal variation in $\langle f_i \rangle$ when plotted as a function of (v_x, v_y) (see Fig. 7, second row) suggests that for the chosen mass ratio, $m_i/m_e = 25$, the magnetized-ion treatment is more applicable than the unmagnetized-ion treatment. Note that in the limit where ions are completely unmagnetized, all diffusion would happen along the v_y direction—hence the choice of mass ratio can determine whether magnetized-ion or unmagnetized-ion quasilinear treatment is more appropriate. The lack of azimuthal variation also confirms that treating each magnetized species' spatially averaged background distribution function as being independent of gyrophase, as done in the linear analysis in Sec. III and in the quasilinear analysis in Sec. IV, is justified. Likewise, ignoring displacement in v_x, as done in the quasilinear analysis, also appears to be justified since spatially averaged distribution functions largely retain their original centroid.

Ion distribution function behavior in the Vlasov simulation can be explained in part by resonant plasma-wave interactions at phase velocities associated with the instability. When a particle trajectory passes through the resonance region (between the blue and red line in contour plots in Figs. 7 and 8), it receives a kick either in the $+v_y$ or $-v_y$ direction for every wave it encounters, which leads to a deformation of its orbit. The larger the amplitude of the wave, i.e., the larger the electric-field energy, the larger the kick. In the ion distribution function evolution (Fig. 7, top row), the kicks are evidenced by petal-like features and initially the number of petals corresponds roughly to $|\omega_{R1}/\Omega_i|$, where ω_{R1} is the real frequency of the fastest-growing mode. The aggregate effect of these particle-wave interactions and orbit deformations, leads to outward diffusion of the spatially averaged distribution function (Fig. 7, bottom row). The observed ion behavior is consistent with theoretical description of stochastic ion heating by a single large-amplitude lower hybrid wave [21] (recall that for diffusion to be applicable, either wave amplitude has to be sufficiently large or the Chirikov criterion must be satisfied). Resonant particle-wave interactions do not straightforwardly explain the electron distribution function evolution (Fig. 8, top row), which is more nuanced. Nonresonant electrons undergo rapid coherent oscillations in response to the fluctuating LHDI-amplified electric field. The associated amplification of electron kinetic energy is evidenced by a broadening of the spatially averaged electron distribution function (Fig. 8, bottom row). See Refs. [25,26,57–59] regarding nonresonant particle-wave interactions and how they relate to temperature and entropy.

D. Diffusion coefficient structure

Since the magnetized-ion quasilinear treatment was found to have a more accurate representation of ion distribution function evolution, we will henceforth focus on the

magnetized-ion calculation. To facilitate comparisons to the magnetized-ion quasilinear calculation, wherein distribution functions are a function of the $v_\perp$ velocity coordinate, the spatially averaged sinc-perturbation Vlasov simulation distribution functions (second row in Figs. 7 and 8) are mapped from (v_x, v_y) velocity coordinates to $(v_\perp, \theta)$ velocity coordinates and averaged over θ. Figure 9 shows the spatially averaged species distribution function as a function of the $v_\perp$ velocity coordinate from the Vlasov simulation, the spatially averaged background species distribution function from the quasilinear calculation, and the normalized species diffusion coefficient from the quasilinear calculation. Each column in Fig. 9 corresponds to a single snapshot in time. Due to different time-step sizes, each snapshot is not exactly aligned between Vlasov simulation and quasilinear calculation, but are very close. Note that quasilinear calculation results in Fig. 9 show a background spatially averaged distribution function and Vlasov simulation results correspond to a spatially averaged background-plus-fluctuations distribution function. We do not apply a temporal average to the Vlasov simulation data since changes in the distribution function occur rapidly during the linear-to-nonlinear transition and the choice of averaging window would significantly affect results.

Figure 9 illustrates that the quasilinear calculation successfully captures the localized deformation of both the ion and electron distribution functions, up to a point. In particular, the quasilinear diffusion coefficient for each species accurately predicts the velocity space regions of largest diffusion and deformation in the Vlasov simulation. Notably, sloshing fluctuations in the Vlasov simulation distribution functions lead to nonmonotonic features, whereas quasilinear calculation distribution functions are monotonic for all time. Late in time, ion distribution function dynamics around $v_\perp = 0$ are not well captured by the quasilinear calculation because one-dimensional diffusion is no longer an adequate description. Interestingly, the quasilinear description appears to capture the global features of the distribution function even when the electron distribution function has evolved significantly away from the initial condition. This is in contrast to the findings in Ref. [24] for bump-on-tail instability, where quasilinear theory was found to be predictive of very small changes in the distribution function.

An effective species diffusion coefficient can be recovered from Vlasov simulation data by solving Eq. (33) for D_{vs}^{mag}. This is done at every velocity coordinate $v_\perp'$ by evaluating $\partial f_s/\partial t$ and $\partial f_s/\partial v_\perp$ using discrete finite differences, multiplying Eq. (33) by $v_\perp$, and integrating over the interval $[0, v_\perp']$. Figure 9 shows the species diffusion coefficient from the Vlasov simulation alongside the quasilinear diffusion coefficient. In evaluating the effective diffusion coefficient in this way, it is implicitly assumed that the diffusion description is applicable, even though it may not be. Figure 10 shows the normalized species diffusion coefficient as a function of velocity and time from the Vlasov simulation and from the quasilinear calculation. In each contour plot in Fig. 10, at each point in time, the species diffusion coefficient is normalized to $\max_{v_\perp \in [0, 0.25 v_{\text{max}}]} D_{vs}^{\text{mag}}(v_\perp, t)$ to clearly show the velocity-space structure, which would otherwise be obscured by exponential growth in time. Note that because the velocity derivative $\partial f_s/\partial v_\perp$ is close to zero at large velocities, the
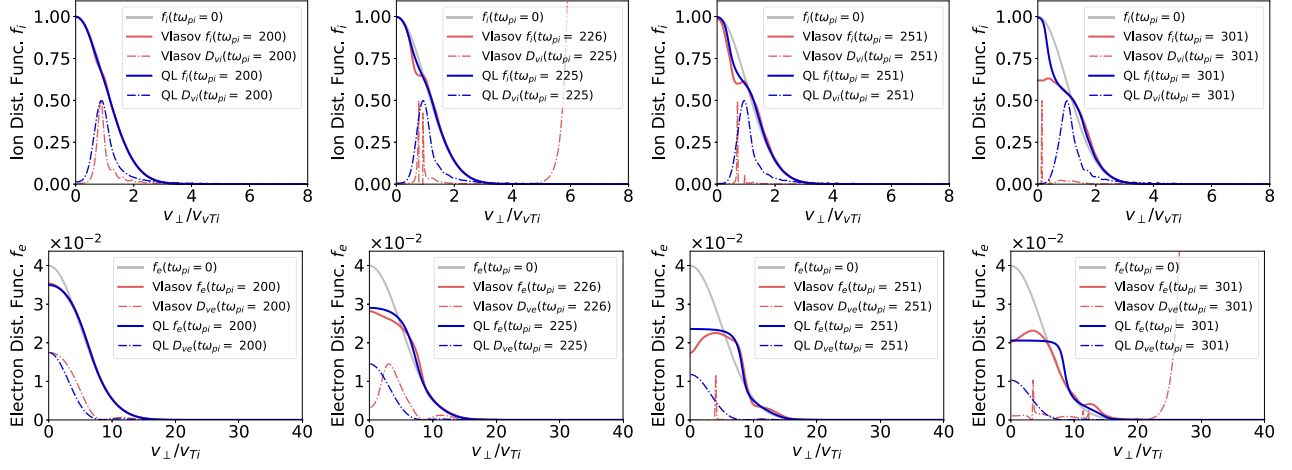
FIG. 9. The spatially averaged distribution function as a function of $v_\perp$ from a magnetized-ion quasilinear calculation and from Vlasov simulation. Also plotted is the diffusion coefficient from the quasilinear calculation and from the Vlasov simulation, both scaled to half of the maximum value of the quasilinear distribution function. The quasilinear description successfully captures the changes in the species distribution functions, up until the point where Vlasov simulation distribution functions become nonmonotonic. At this point diffusion does not adequately describe dynamics in the Vlasov simulation.

effective species diffusion coefficient from the Vlasov simulation takes on disproportionately large values in these regions, whereas the bulk of the diffusive action is actually at smaller $v_\perp$ velocities. Consequently, Vlasov simulation contour plots in Fig. 10 are capped at a value of unity.

Figure 10 shows that during the linear stage and the initial transition to the nonlinear regime (i.e., up to time of about $t\omega_{\mathrm{pi}} = 220$), the species-specific diffusion coefficient structure in the Vlasov simulation and quasilinear calculation are very similar. However, at some point the diffusion description
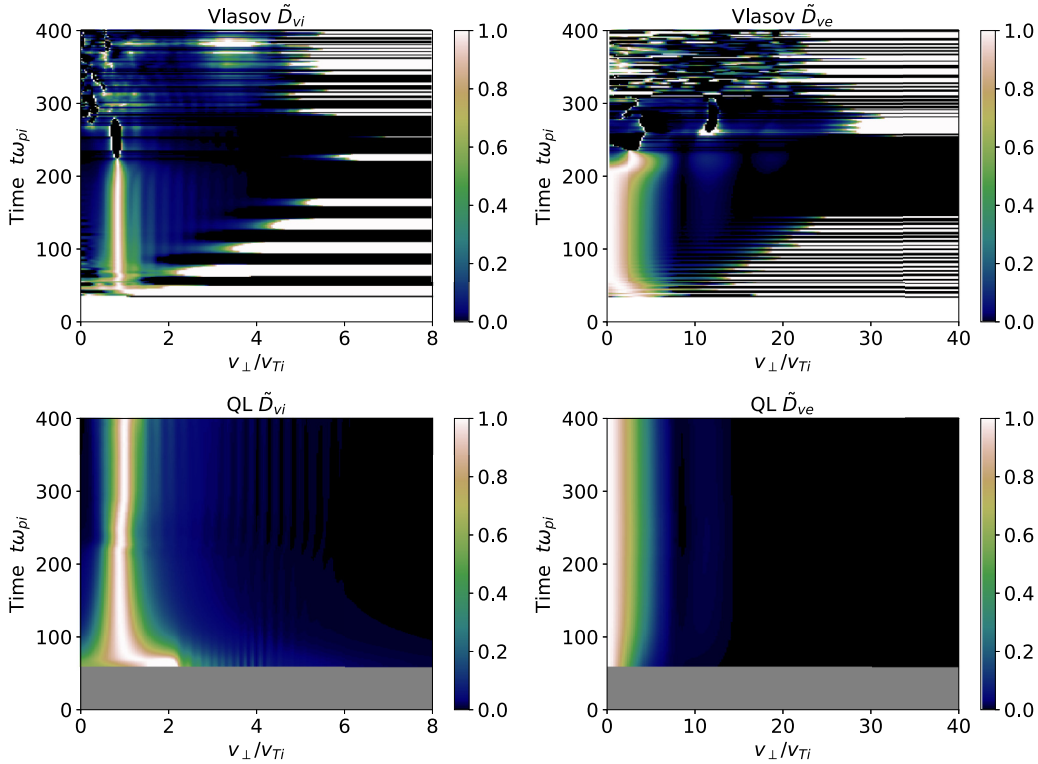

FIG. 10. Effective ion and electron diffusion coefficients from Vlasov simulation (top row) and species diffusion coefficient from the magnetized-ion quasilinear calculation (bottom row). At every point in time the diffusion coefficients are normalized to $\max_{v_\perp \in [0, 0.25 v_{\max}]} D_{vs}^{\mathrm{mag}}(v_\perp, t)$ to clearly show the velocity-space structure as a function of time. Vlasov simulation diffusion coefficient contours are capped at unity. These results illustrate that up to time $t\omega_{\mathrm{pi}} \approx 220$ the velocity-space structure of the diffusion coefficient is largely captured by the quasilinear calculation. Gray regions signify no data due to time shift of quasilinear calculation to align with Vlasov simulation time history.

is no longer applicable in the Vlasov simulation, as evidenced by the effective diffusion coefficient becoming discontinuous in time and in velocity. At this point, distribution function evolution is characterized more by back-and-forth sloshing rather than by diffusion. By contrast, diffusion continues indefinitely in the quasilinear calculation, due to the fact that for some time-evolving set of wave numbers, growth rate ω_I (and hence diffusion) is strictly greater than zero for all time. Notably, the effective electron diffusion coefficient in the Vlasov simulation undergoes a rapid change in structure around time $t\omega_{\mathrm{pi}} = 220$, which is not reflected in the quasilinear calculation, wherein the structure of the electron diffusion coefficient remains largely unchanged.

Overall, results in Figs. 9 and 10 illustrate that one-dimensional diffusion, as described by quasilinear theory, provides a predictive description of the nonlinear dynamics of the two-species acceleration-driven LHDI—up to a point. The point of failure can be quantified in the Vlasov simulation by evaluating an effective diffusion coefficient and tracking where it becomes discontinuous, which places an important bound on the applicability of quasilinear theory. A signature of when quasilinear theory is no longer applicable can also be gleaned from the quasilinear calculation itself, as will be shown in Sec. VII E.

E. Anomalous transport

An important practical application of quasilinear theory is predicting anomalous transport [2]. Yet the theory's translation of a nonlinear collisionless kinetic description into anomalous transport terms in a collisional fluid description is only useful so far as it is accurate. Here we examine to what degree the self-consistent quasilinear theory for acceleration-driven LHDI accurately predicts momentum and energy transport.

1. Anomalous momentum transport

LHDI microturbulence affects momentum by producing an effective electron-ion drag, with anomalous electron-ion collision frequency ν_{anom}. This drag, which is a collisional multifluid representation of a collisionless kinetic phenomenon, is commonly expressed as a resistivity in a single-fluid MHD description. In the case of gradient-driven LHDI precipitated by current perpendicular to a background magnetic field, the drag simultaneously causes cross-field diffusion, flattening of the gradient, and a decrease in each species' drift velocity [56]. In the present context, where we examine an acceleration-driven LHDI in a uniform plasma, a species' y-directed drift velocity is largely unaffected by the instability since g_x and B_z are taken to be constant. The main effect of LHDI on momentum is consequently y-directed drag and drag-induced x-directed motion. These changes are accompanied by heating of the plasma.

Taking the first velocity moment of the electron Vlasov equation and evaluating the spatial average of each term as a function of time using Vlasov simulation data, confirms that $\langle q_e n_e E_y \rangle$ (i.e., the drag, according to quasilinear theory) and $\langle q_e n_e u_x B_z \rangle$ are in balance, and other terms have a negligible contribution to the electron momentum equation. See Fig. 11. This balance of terms in the electron momentum equation is
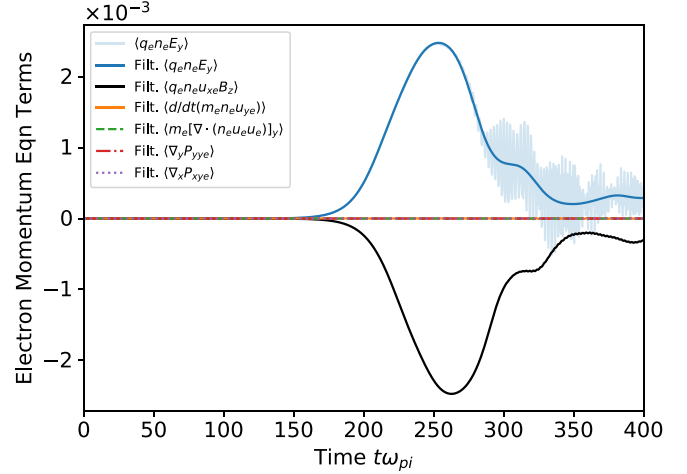

FIG. 11. The balance of volume-average terms in the electron fluid momentum equation, evaluated by taking the first velocity moment of the Vlasov equation using Vlasov simulation data. The time history shows that the quasilinear drag force, $\langle q_e n_e E_y \rangle$, and $\langle q_e n_e u_{xe} B_z \rangle$ nearly exactly balance each other whereas other terms are negligible, as is expected for a plasma whose dynamics are dominated by electron-ion drag and drag-induced x-directed motion. With the exception of $\langle q_e n_e E_y \rangle$, for which a raw data trace is shown, the evolution of each term is low-pass filtered to show the overall trend. Since the drag force on electrons is negative of that on ions, both species experience the same x-directed velocity u_{xs}. In resistive MHD terms, the y-directed anomalous resistivity induces x-directed motion perpendicular to the background magnetic field according to the Ohm's law $u_x B_z = \eta_{\mathrm{anom}} j_y$.

consistent with the Ohm's law, $u_x B_z = \eta_{\mathrm{anom}} j_y$, for a resistive magnetohydrodynamic plasma, and gives zeroth order supporting evidence that the quasilinear model's description of plasma dynamics being governed by drag is accurate. The overall trend in the time history shown in Fig. 11, wherein $\langle q_e n_e E_y \rangle$ reaches a maximum and subsequently decreases, is characteristic of all Vlasov simulations we have conducted and appears to be independent of the choice of parameters and initial conditions.

The LHDI-induced collision frequency ν_{anom} [see Eq. (41) and surrounding text] is plotted as a function of time in Fig. 12—from the Vlasov simulation, the magnetized-ion quasilinear calculation, and the unmagnetized-ion quasilinear calculation. This anomalous collision frequency is computed as

$$\nu_{\mathrm{anom}} = \frac{F_d}{m_e(n_e u_{ye} - n_i u_{yi})}, \qquad (55)$$

with drag force per unit volume F_d evaluated as $\langle q_e n_e E_y \rangle$ in the Vlasov simulation and evaluated using Eq. (41) in the quasilinear calculations. Note that u_{ye} and u_{yi} are constant in the quasilinear description, such that ν_{anom} is simply proportional to the drag force.

Up to time of about $t\omega_{\mathrm{pi}} = 250$, the time evolution of anomalous collision frequency follows the same qualitative trend in all the models: monotonic increase up to a peak value, followed by a decrease. For $t\omega_{\mathrm{pi}} > 250$, when quasilinear diffusion is no longer an accurate approximation, the models exhibit significant deviations: ν_{anom} from the Vlasov
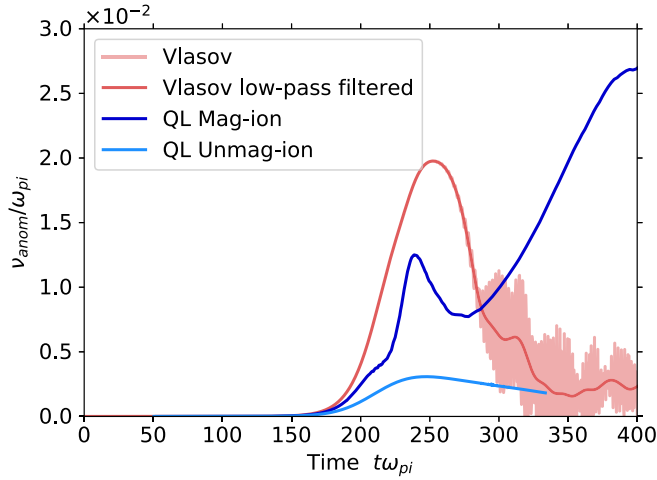
FIG. 12. Time evolution of anomalous collision frequency ν_{anom}, defined in Eq. (55), due to the acceleration-driven LHDI. The collision frequency is computed from the Vlasov simulation, the magnetized-ion quasilinear calculation, and the unmagnetized-ion quasilinear calculation data. Up to time $t\omega_{\text{pi}} \approx 250$ the magnetized-ion quasilinear treatment better captures the evolution of ν_{anom}, but significantly underestimates the anomalous collision frequency. The time at which ν_{anom} initially peaks can be used as a measure of when quasilinear theory is no longer valid.

simulation and unmagnetized-ion quasilinear calculation continues to decline, whereas ν_{anom} from the magnetized-ion quasilinear calculation increases to a larger value. The initial peak value of ν_{anom} occurs roughly at the same point in time for all the models—$t\omega_{\text{pi}} \in [240, 250]$. This point roughly coincides with the time at which quasilinear diffusion stops being applicable (see Fig. 10) and occurs when electric-field energy growth rate has decreased to about 10% of the peak growth rate value. This initial peak in $\nu_{\text{anom}}(t)$ provides a signature of when the quasilinear description ceases to be valid. The peak value is also of interest when trying to develop models for use in fluid codes, in which anomalous collision frequency is typically described as a function of local plasma temperature, drift velocity, etc. Early in time, the anomalous collisionality increases because of mode growth, while at times after the peak the presence of microinstability has strongly distorted and raised the "temperature" of the distribution functions such that anomalous collisionality weakens. The initial peak drag is at a time when the modes have grown to a high value yet the distribution function has not yet strongly deviated from the original plasma parameters, hence is most relevant to a local anomalous collisionality described as a function of those parameters.

Quantitatively, quasilinear predictions of ν_{anom} disagree with Vlasov simulation results. Using the initial peak value of $\nu_{\text{anom}}(t)$ as a reference point, the unmagnetized-ion quasilinear calculations underpredicts the Vlasov collision frequency by about a factor of five and the magnetized-ion quasilinear calculation underpredicts the Vlasov collision frequency by about 30%. These results underscore that treating the ions as magnetized is a better approximation for the parameter case under consideration. Interestingly, the discrepancies between the Vlasov ν_{anom} and magnetized-ion quasilinear ν_{anom} are substantially larger than the discrepancies between

the electric-field energies predicted by the two models. This means that even when quasilinear calculations can accurately predict the saturated electric-field energy (see electric field energy evolution in Fig. 5 around $t\omega_{\text{pi}} = 240$), this does not necessarily translate to accurate prediction of anomalous collision frequency and momentum transport (see Fig. 12). The reason for this has to do with the fact that the time evolution of ν_{anom} depends on the time evolution of both $\mathcal{E}_k(k, t)$ and $\text{Im}[\chi_s(k, t)]$—see Eqs. (41) and (55) for how these variables are related. As $\mathcal{E}_k(k, t)$ increases in time, the magnitude of the imaginary part of the species susceptibility $|\text{Im}[\chi_s(k, t)]|$ decreases in time and decreases more rapidly at the linear-to-nonlinear transition. Inaccuracy in the linear-theory susceptibility χ_s can thus lead to inaccuracy of quasilinear theory's prediction of anomalous collision frequency. This suggests that the use of unperturbed-orbit susceptibilities (characteristic of any linear-theory dispersion relation) in the quasilinear model can lead to inaccuracies in anomalous transport terms. Notably, the limitations of using linear-theory dispersion relations in the context of nonlinear kinetic turbulence theories have been conjectured since the 1960s [23,60].

2. Energy balance and anomalous heating

LHDI microturbulence causes a redistribution of plasma energy and associated heating of electrons and ions. In the kinetic picture, plasma-wave interactions lead to outward velocity-space diffusion and associated heating of each distribution function. In a fluid interpretation, the LHDI-induced anomalous collision frequency ν_{anom} and associated resistivity lead to joule heating of the plasma.

The change in the different types of energy densities in the Vlasov simulation and magnetized-ion quasilinear calculation are shown in Fig. 13. Noticeable changes in energy balance occur when the instability transitions from the linear to the nonlinear regime around $t\omega_{\text{pi}} = 200$. While energy distribution in the Vlasov simulation and quasilinear calculation exhibit similar trends, they do not match quantitatively. In both models the increase in thermal energy comes at the expense of the gravitational energy, i.e., the potential energy associated with constant acceleration. Energy associated with y-directed drift motion is constant in the quasilinear model and is nearly constant with a sinusoidal ion-gyroperiod oscillation in the Vlasov simulation. Figure 13 also shows that the contribution of electric-field energy to the total energy is almost negligible—quantitatively less than one tenth of one percent in both models. The plot in Fig. 13 confirms the fact that electric-field energy is much smaller than thermal energy, specifically, which was one of the requirements for quasilinear theory to be applicable. Total energy in the Vlasov simulation (which includes gravitational, electric-field, x-directed drift, y-directed drift, and thermal) is conserved to within 0.02% of the initial total energy. Total energy in the quasilinear calculations (which includes gravitational, electric-field, y-directed drift, and thermal) is conserved to within 0.00002% of the initial total energy. Interestingly, in the Vlasov simulation x-directed drift energy grows from zero to a value on par with electric-field energy—a physical feature that is not captured by the quasilinear model.
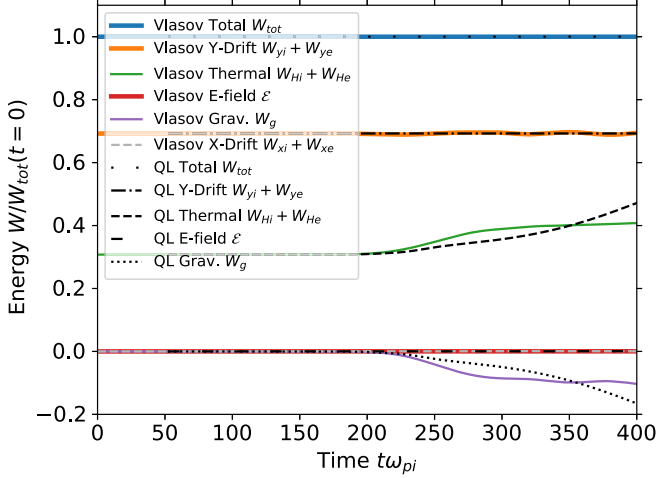
FIG. 13. Energy balance in the Vlasov simulation and the magnetized-ion quasilinear calculation for the acceleration-driven LHDI. Each type of energy is plotted relative to the initial-time total energy $W_{\text{tot}}(t = 0)$. The quasilinear model successfully captures the main trends: nearly constant y-directed drift energy, decrease in gravitational energy, increase in thermal energy, conservation of total energy, and negligible change in electric-field energy when compared to thermal energy. Quantitatively, the two models deviate significantly, particularly late in time when the Vlasov simulation appears to reach a steady state while the quasilinear calculation energy densities continue to evolve. The x-directed drift energy is small and finite in the Vlasov simulation and is exactly zero in the quasilinear model.

The distribution of thermal energy among the two species is also of interest. Figure 14 shows the heating rate of ions and electrons in the Vlasov simulation, in the magnetized-ion quasilinear calculation, and in the unmagnetized-ion quasilin-
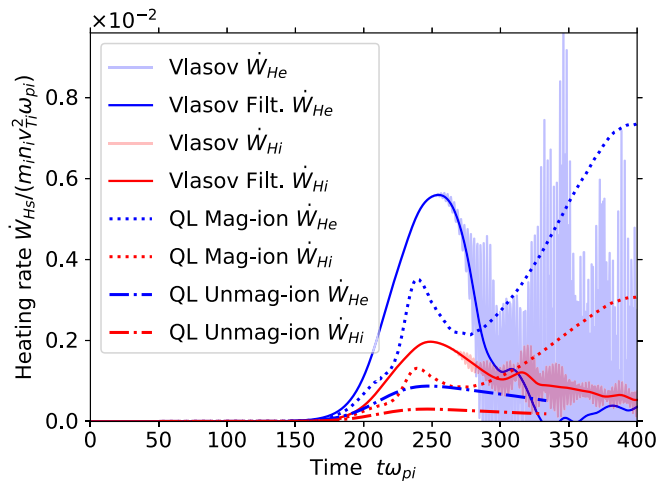

FIG. 14. Species anomalous heating rates in Vlasov simulation (unfiltered data and low-pass filtered data), magnetized-ion quasilinear calculation, and unmagnetized ion quasilinear calculation. Quasilinear calculations underpredict the heating rates observed in Vlasov simulations, particularly when ions are treated as unmagnetized and electric-field energy density at saturation is likewise underpredicted, as shown in Fig. 5.
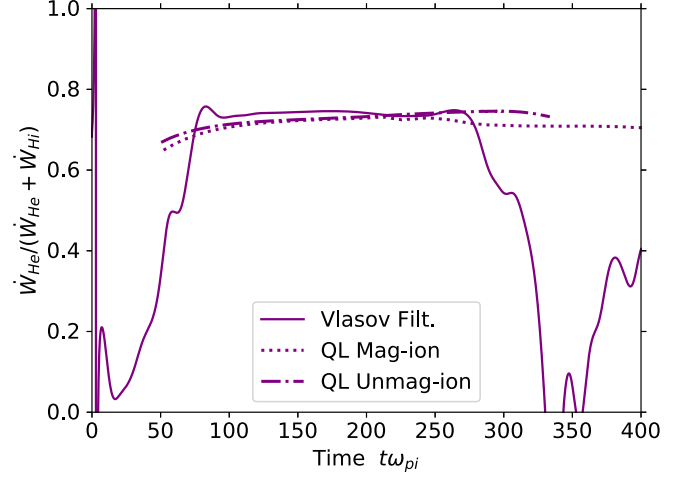

FIG. 15. Fractional electron heating induced by the acceleration-driven LHDI, according to Vlasov simulation, magnetized-ion quasilinear calculation, and unmagnetized-ion quasilinear calculation. All of the models predict roughly a constant fractional electron heating rate that is close to 70% of the total heating rate. Thus, even in cases where species heating rates are significantly underpredicted by the quasilinear description (see Fig. 14), the fractional heating rates can be much more accurate.

ear calculation. In the Vlasov simulation, the species heating rate is computed as the time derivative of thermal energy, which is obtained from velocity moments of the distribution function. In the quasilinear calculation, the species heating rate is evaluated using Eq. (43). The same level of discrepancy observed in ν_{anom} between the Vlasov simulation and quasilinear calculations is present in the species heating rates, which is expected since heating is proportional to the drag force F_{ds}. Specifically, the magnetized-ion quasilinear model is a better predictor of species heating, but is only accurate to within a factor of two.

The fractional heating rate, which indicates what fraction of the total heating goes into heating the electrons, is also of interest and is better captured by the quasilinear description. Figure 15 shows the ratio of electron heating to the total heating rate of the plasma. For the time duration over which a quasilinear diffusion description is applicable, the fractional electron heating rate is effectively constant in time and has a value that is approximately consistent between all the models, such that about 70% of the instability-induced heating goes into heating electrons and the rest into ions. The result that electrons heat faster than ions for a $T_i/T_e = 1$ plasma is consistent with previous quasilinear and reduced-model analysis of the gradient-driven LHDI [2,14] as well as other drift-driven kinetic instabilities [61].

Fractional heating aside, the results presented in Figs. 5, 12, and 14 suggest that even if the prediction of the saturated electric-field energy value is accurate (as in the magnetized-ion quasilinear treatment), quasilinear calculations cannot predict anomalous transport properties to an accuracy that is better than a factor of two. When the electric-field energy at saturation is not accurately predicted (as in the unmagnetized-ion quasilinear treatment), then the accuracy of anomalous transport predictions

diminishes further. The discrepancies between Vlasov simulations and quasilinear calculations are likely due to linear-theory susceptibilities becoming inaccurate during the linear-to-nonlinear transition. Discrepancies can also be attributed to nonlinear damping, which is not captured by the quasilinear description. The limitations of a complete quasilinear theory, such as the one presented here, bring into question the accuracy of transport predictions from more common quasilinear models that rely on further simplifications. Nevertheless, given that anomalous resistance can be orders of magnitude larger than classical resistance, factor-of-two level of accuracy can yield powerful and insightful transport predictions.

VIII. CONCLUSIONS

We have successfully derived a complete self-consistent two-species quasilinear velocity-space diffusion model for describing the nonlinear physics of the acceleration-driven LHDI in a uniform low-beta plasma. The model contains less information and less degrees of freedom than a Vlasov-Poisson description of the instability, but still encapsulates the average effect of nonlinear collisionless kinetic physics on bulk fluid transport properties of the plasma. The model has several unique features that make it more general than existing quasilinear theory descriptions of LHDI and other instabilities. These features are related to the form of the dispersion relation and to the mathematical form of the diffusion coefficient. Specifically: (1) The dispersion relation applies to arbitrary (Maxwellian or non-Maxwellian) distribution functions, as long as they can be expressed as a function of a single velocity coordinate (v_y or $v_\perp$). The dispersion relation is not constrained to asymptotic limits for dimensionless parameters Ω_e/ω_{pe}, T_i/T_e, m_i/m_e, and $k_y r_{Le}$. Furthermore, rather than being expressed in summation form, as is common practice, the dispersion relation is expressed in integral form, which facilitates accurate evaluation without introducing truncation errors. (2) The quasilinear diffusion model accounts for both resonant and nonresonant particle-wave interactions. (3) The model also accounts for multiple species, which can be treated as magnetized or unmagnetized. (4) Importantly, because spectral density of the electric-field energy per unit volume and distribution functions have self-consistent evolution equations that encapsulate the time-evolving diffusion coefficient and mixed-complex frequency, the model does not rely on heuristic rules for predicting the saturated nonlinear state of the plasma. (5) The model conserves energy and can be used to obtain anomalous momentum and energy transport terms for fluid equations using wave-number- and time-dependent species susceptibilities and spectral density of the electric-field energy.

We have presented a methodology for solving the quasilinear theory system of governing partial differential equations. The numerical solver is based on a second-order Crank-Nicholson time advance method coupled with a second-order finite-volume velocity space discretization. Efficient means of solving the dispersion relation numerically, based on the Nyquist method and the Levenberg-Marquardt algorithm, are described. The numerical solver efficiency is improved through the use of adaptive time steps and parallelization in wave number.

The quasilinear model's predictive capabilities are assessed by comparing numerical solutions of the quasilinear model to numerical solutions of the Vlasov-Poisson equation system. Numerical solutions of the Vlasov-Poisson equation system are obtained using VCK, a benchmarked parallel conservative continuum kinetic fourth-order finite-volume solver. Due to the computational cost of Vlasov simulations, a mass ratio of $m_i/m_e = 25$ is used, for which a magnetized-ion and magnetized-electron quasilinear treatment is found to be more predictive.

Numerical results demonstrate that the quasilinear model is effective at predicting volume-average plasma behavior, including: electric-field energy evolution and magnitude, the relative importance of different wave-number modes, the velocity-space structure of the species diffusion coefficients and distribution functions, and the qualitative energy and momentum balance associated with the nonlinear stage of the acceleration-driven LHDI. The model is less predictive of anomalous transport properties, like anomalous collision frequency and anomalous species heating rate, which rely on the correctness of both the spectral density of the electric-field energy and the species susceptibilities. The quasilinear model predicts anomalous transport terms to within a factor of two, up until the time at which anomalous collision frequency peaks. The peak in the time-dependent anomalous collision frequency, or equivalently a peak in the drag force, is identified as a signature of when a quasilinear diffusion description is no longer valid according to Vlasov simulations.

Discrepancies between the quasilinear model and the Vlasov-Poisson description are expected and can be attributed to several factors. First, the quasilinear description considers a continuous wave-number spectrum for an infinite-domain plasma, whereas Vlasov simulations capture a discrete wave-number spectrum for a periodic-domain plasma, which results in different modes in the two models. The quasilinear model description ignores certain physics, including dependence of the average distribution function on the gyrophase and changes in drift velocity, both of which are observed in Vlasov simulations. Likewise, the quasilinear description does not incorporate nonlinear damping physics, which is evident in Vlasov simulations. The use of unperturbed-orbit susceptibilities (which account for changes to the distribution function, but still treat all magnetized-species trajectories as circles) in the quasilinear model can be problematic, as evidenced by the fact that the model is more predictive of electric-field energy than of anomalous transport terms. This constitutes an important nonlinearity that is not captured in the quasilinear model. A well-known limitation is that the quasilinear model neglects nonlinearities associated with wave-wave interactions, which, although not evidenced in the present study, can also potentially affect instability evolution.

The present study was limited in scope in that it did not exhaustively explore the vast parameter space associated with the acceleration-driven LHDI, including different T_i/T_e, m_i/m_e, Ω_e/ω_{pe}, V_d/v_{Ti} ratios. In particular, it remains to be seen whether the results here extend to more realistic mass ratios and multiple ion species. Likewise, the study did not explore the vast space of numerical solver parameters

available, including domain size in velocity space, domain size in wave-number space, resolution, tolerances, etc., all of which can potentially affect the accuracy of quasilinear calculations. Such studies are left as a topic for future work. Another limitation is the lack of a grid convergence study for the Vlasov simulations. A convergence study, which can be facilitated by more compute resources and/or code performance optimization, would provide a rigorous measure of how close simulations are to the true solution. This is also left as a topic for future work.

Beyond its validity and accuracy, it is also important to factor in the computational cost of the quasilinear model. While the quasilinear model has less degrees of freedom than a Vlasov-Poisson simulation and can be trivially parallelized in wave number, it is still computationally expensive to solve—primarily because it requires iteratively solving the dispersion relation at every time step and every wave number. For the calculations conducted here, Vlasov simulations were ran on 9216 cores and the quasilinear calculations (which were not optimized for performance) were ran on 56 cores—both took about 24 hours. Therefore, the quasilinear model presented here does not provide compute-time savings, but can provide larger throughput of calculations and more expedient parameter space exploration—particularly for realistic mass ratios, which can result in prohibitively expensive Vlasov simulations. Quasilinear calculations can thus be used to predict nonlinear physics in parameter regimes that are otherwise, due to limits of today's Vlasov solvers, difficult or impossible to access. A quasilinear-model mapping from local plasma parameters to nonlinear conditions can facilitate efficient anomalous transport models for global fluid-based simulations of experiments. Because changes in parameters would still have to be vetted against Vlasov simulations, the quasilinear model described here is unlikely to serve as a reliable substitute to nonlinear kinetic simulations. The quasilinear model does, however, provide valuable theoretical insights into nonlinear physics that can be difficult to glean from Vlasov simulations. Of particular value is the insight into the velocity-space structure of each species' diffusion coefficient and how it depends on the plasma state—an important mathematical link between linear- and nonlinear-regime physics.

The present results provide a rigorous assessment of a complete quasilinear model for a nonlinear acceleration-driven lower hybrid instability in a magnetized low-beta multispecies collisionless plasma. The limitations of the theory suggest that quasilinear models, especially those that are incomplete or rely on additional approximations to infer saturated state conditions, can be expected to give at best only order-of-magnitude accuracy for transport predictions. Quantitative bounds on quasilinear theory's applicability, such as those explored here, warrant further investigation and provide much needed vetting of quasilinear descriptions for anomalous transport.

APPENDIX A: LINEAR KINETIC THEORY DISPERSION RELATION DERIVATION DETAILS

In using Eq. (20) expression for $\hat{f}_{s1}$ and the linearized Poisson equation to derive a dispersion relation, the objective is to arrive at an integral form expression to avoid infinite sums and to facilitate accurate numerical solutions. The mathematical manipulations used here are largely based on the analysis presented in Ref. [34]. Starting with the expression in Eq. (20), using the variable substitution $\psi = \theta - \tau/2$, rewriting $\cos(\psi - \frac{\tau}{2})$ as $\cos\psi\cos(\frac{\tau}{2}) + \sin\psi\sin(\frac{\tau}{2})$, and averaging over the gyrophase angle ψ (i.e., integrating with respect to ψ over the interval $[0, 2\pi]$ and dividing by 2π) yields

$$\hat{f}_s(k_y, \omega, v_\perp) = -\frac{q_s}{2\pi m_s \Omega_s} \frac{\partial f_{s0}}{\partial v_\perp} \int_0^\infty \left\{ \hat{E}_{1y} \exp\left(i\mathcal{W}\tau\right) \right.$$
$$\times \int_0^{2\pi} \exp\left[-\frac{2ik_y v_\perp}{\Omega_s} \cos(\psi) \sin\left(\frac{\tau}{2}\right) \right]$$
$$\left. \times \left[\cos\psi \cos\left(\frac{\tau}{2}\right) + \sin\psi \sin\left(\frac{\tau}{2}\right) \right] d\psi \right\} d\tau,$$
(A1)

where $\hat{f}_s(k_y, \omega, v_\perp) = \frac{1}{2\pi} \int_0^{2\pi} \hat{f}_s(k_y, \omega, v_\perp, \psi) d\psi$ and where $\mathcal{W}_s = \frac{\omega}{\Omega_s} - \frac{k_y g}{\Omega_s^2}$, as defined in Eq. (21). The $\sin\psi\sin(\frac{\tau}{2})$ term integrates to zero since it is of the form $\int_0^{2\pi} \exp(-ia\cos\psi)d(\cos\psi)$ for constant a. The $\cos\psi\cos(\frac{\tau}{2})$ term can be integrated using the Bessel function identity $J_n(z) = \frac{i^n}{2\pi} \int_0^{2\pi} e^{-iz\cos\psi} \cos(n\psi)d\psi$, where J_n is the Bessel function of the first kind with $n \in \mathbb{Z}$ and $z \in \mathbb{C}$. Equation (A1) can then be expressed as

$$\hat{f}_{s1}(k_y, \omega, v_\perp) = \frac{q_s}{m_s \Omega_s} \frac{\partial f_{s0}}{\partial v_\perp} \int_0^\infty \left\{ \hat{E}_{1y} \exp\left(i\mathcal{W}_s\tau\right) \right.$$
$$\left. \times iJ_1\left(\frac{2k_y v_\perp}{\Omega_s} \sin\left[\frac{\tau}{2}\right] \right) \cos\left(\frac{\tau}{2}\right) \right\} d\tau.$$
(A2)

The integral over $[0, \infty)$ can be replaced by an infinite sum of integrals over the interval $[2\pi n, 2\pi(n + 1)]$ for integer $n = \{0, 1, \cdots\}$. Using the substitution $\phi = \tau - 2\pi n$ and simplifying yields

$$\hat{f}_{s1}(k_y, \omega, v_\perp) = \frac{q_s i}{m_s \Omega_s} \frac{\partial f_{s0}}{\partial v_\perp} \int_0^{2\pi} \left\{ \hat{E}_{1y} \frac{\exp\left(i\mathcal{W}_s\phi\right)}{1 - \exp(2\pi i\mathcal{W}_s)} \right.$$
$$\left. \times J_1\left(\frac{2k_y v_\perp}{\Omega_s} \sin\left[\frac{\phi}{2}\right] \right) \cos\left(\frac{\phi}{2}\right) \right\} d\phi.$$
(A3)

Substituting Eq. (A3) into the linearized Poisson equation,

$$k_y^2 \hat{\Phi}_1 = \frac{1}{\epsilon_0} \sum_s q_s \int_0^\infty \hat{f}_{s1} v_\perp dv_\perp,$$
(A4)

noting that $\hat{E}_{1y} = -ik_y\hat{\Phi}_1$ and applying integration by parts yields the dispersion relation given in Eq. (22), with susceptibilities defined in Eq. (23).

APPENDIX B: COLD-FLUID LINEAR THEORY FOR THE ACCELERATION-DRIVEN LHDI

Interestingly, some features of the acceleration-driven LHDI can be recovered even in the cold-fluid limit—a regime in which kinetic theory and fluid theory are exactly consistent. The linearized continuity and momentum equations for a zero-temperature fluid species in the presence of a gravitylike force are

$$0 = \frac{\partial n_{s1}}{\partial t} + n_{s0} \nabla \cdot \boldsymbol{u}_{s1} + \boldsymbol{u}_{s0} \cdot \nabla n_{s1}, \tag{B1}$$

$$0 = m_s n_{s0} \frac{\partial \boldsymbol{u}_{s1}}{\partial t} + m_s n_{s0} \boldsymbol{u}_0 \cdot \nabla \boldsymbol{u}_{s1} - q_s (n_{s0} \boldsymbol{E}_1 + n_{s0} \boldsymbol{u}_{s1}$$
$$\times \boldsymbol{B}_0 + n_{s1} \boldsymbol{u}_{s0} \times \boldsymbol{B}_0) + m_s n_{s1} g, \tag{B2}$$

where $\boldsymbol{u}_{s0}$ is the equilibrium species drift velocity and $\boldsymbol{u}_{s1}$ is the perturbed velocity. Assuming waveform solutions, e.g., $n_1 = \hat{n}_1 \exp(i[\boldsymbol{k} \cdot \boldsymbol{x} - \omega t])$, solving for $\hat{n}_{s1}$, using the linearized Poisson equation, and noting that equilibrium drift velocity is $u_{s0y} = g/\Omega_s$ yields the cold-fluid dispersion relation for the acceleration-driven LHDI,

$$0 = 1 + \frac{\omega_{pi}^2/\Omega_i^2}{1 - \left(\frac{\omega}{\Omega_i} - \frac{k_y g}{\Omega_i^2}\right)^2} + \frac{\omega_{pe}^2/\Omega_e^2}{1 - \left(\frac{\omega}{\Omega_e} - \frac{k_y g}{\Omega_e^2}\right)^2}. \tag{B3}$$

The dispersion relation in Eq. (B3) captures the effects of mass ratio and magnetization level as measured by ω_{ps}/Ω_s ratio, but does not encapsulate scales associated with thermal speed and Larmor radius, which are captured by the full kinetic theory analysis in Eqs. (1) to (26). Cold-fluid theory does not capture the fact that as the ratio of drift velocity $V_d = u_{yi} - u_{ye}$ to thermal speed decreases, the instability growth rate decreases. Consequently, for a finite-temperature plasma, cold-fluid growth rates can far exceed kinetic theory growth rates.

APPENDIX C: TIME-STEP SIZE, MASS RATIO, AND COMPUTATIONAL COST

Realistic mass ratios significantly limit the time-step size in Vlasov simulations, particularly for multispecies simulations that include electron dynamics. Vlasov simulations use explicit RK4 time advance and are subject to the Courant–Friedrichs–Lewy (CFL) condition. For the 3D (y, v_x, v_y) phase space dynamics under consideration, the con-

straint on time-step size is

$$\Delta t \leqslant \sigma \cdot \min \left\{ \frac{h_y}{v_{y,\max}}, \frac{h_{v_x}}{\max|a_x|}, \frac{h_{v_y}}{\max|a_y|} \right\},$$
$$a_x = \frac{q_s}{m_s}(E_x + v_y B_z) - g_x, \tag{C1}$$
$$a_y = \frac{q_s}{m_s}(E_y - v_x B_z),$$

where σ is a dimensionless Courant number with $\sigma \lesssim 0.6$ for the finite-volume method used [38,55], and $\{h_y, h_{v_x}, h_{v_y}\}$ are the cell spacings along each coordinate direction. The maximum/minimum values are taken over phase space and over species, such that electrons tend to restrict the time step more severely. For the acceleration-driven LHDI, the magnetic field term is the largest-magnitude term in a_x and a_y. Note that for $T_e = T_i$, a decrease in electron mass relative to ion mass results in a relative increase in electron thermal speed, which requires extending the velocity domain, nominally by $(m_i/m_e)^{1/2}$. Thus, the time-step size scales roughly as $(m_i/m_e)^{3/2}$, which means that for a fixed cell spacing, a simulation with $m_i/m_e = 1836$ would be about 630 times slower than a $m_i/m_e = 25$ simulation. However, for a fixed number of cells, a Vlasov simulation with $m_i/m_e = 1836$ would be about 73 times slower than a $m_i/m_e = 25$ simulation. Depending on the choice of dimensionless parameters, a larger mass ratio can also result in smaller peak growth rates, which can further extend the compute time needed to run a simulation.

In the quasilinear diffusion model, which uses an implicit unconditionally stable Crank-Nicolson time advance, the time-step size is nominally subject to the constraint $\Delta t \lesssim \frac{1}{2}\min(\frac{h_v^2}{D_{v_s}})$ to avoid spurious oscillations. Here h_v is the cell spacing and the minimum value is over velocity space and over species. The time-step size is thus independent of mass ratio. Mass ratio can come into play indirectly through the diffusion coefficient, e.g., resolving the structure of the each species' diffusion coefficient to accurately compute the integral in Eq. (34) (see Fig. 4) in a realistic mass-ratio magnetized-ion plasma can require orders of magnitude more wave-number resolution. This computational expense can be ameliorated by parallelizing further in wave-number space and by using the unmagnetized-ion susceptibility, which results in smoother $\omega_I(k_y)$ (see Figs. 2 and 3) and thereby smoother (in wave-number) diffusion coefficient integrands $D_{vsk}(\boldsymbol{v}, k_y)$. As with Vlasov simulations, realistic mass ratios can result in smaller peak growth rates, which can extend the quasilinear solver calculation time.

[1] N. A. Krall and P. C. Liewer, Low-frequency instabilities in magnetic pulses, Phys. Rev. A **4**, 2094 (1971).

[2] R. C. Davidson and N. T. Gladd, Anomalous transport properties associated with the lower-hybrid-drift instability, Phys. Fluids **18**, 1327 (1975).

[3] D. Winske, Short-wavelength modes on expanding plasma clouds, J. Geophys. Res. **93**, 2539 (1988).

[4] D. Winske, Development of flute modes on expanding plasma clouds, Phys. Fluids B **1**, 1900 (1989).

[5] R. Davidson and N. Krall, Anomalous transport in high-temperature plasmas with applications to solenoidal fusion systems, Nucl. Fusion **17**, 1313 (1977).

[6] D. D. Ryutov, M. S. Derzon, and M. K. Matzen, The physics of fast Z pinches, Rev. Mod. Phys. **72**, 167 (2000).

[7] M. Tanaka and T. Sato, Simulations on lower hybrid drift instability and anomalous resistivity in the magnetic neutral sheet, J. Geophys. Res. **86**, 5541 (1981).

[8] G. T. Birk and A. Otto, The resistive tearing instability for generalized resistivity models: Applications, Phys. Fluids B **3**, 1746 (1991).

[9] P. H. Yoon and A. T. Y. Lui, Anomalous resistivity by fluctuation in the lower-hybrid frequency range, J. Geophys. Res. A: Space Phys. **112** (2007).

[10] D. B. Sinars, M. A. Sweeney, C. S. Alexander, D. J. Ampleford, T. Ao, J. P. Apruzese, C. Aragon, D. J. Armstrong, K. N. Austin, T. J. Awe, A. D. Baczewski, J. E. Bailey, K. L. Baker, C. R. Ball, H. T. Barclay, S. Beatty, K. Beckwith, K. S. Bell, J. Benage, J. F. Benage, Jr., N. L. Bennett *et al.*, Review of pulsed power-driven high energy density physics research on Z at Sandia, Phys. Plasmas **27**, 070501 (2020).

[11] M. R. Gomez, R. M. Gilgenbach, M. E. Cuneo, C. A. Jennings, R. D. McBride, E. M. Waisman, B. T. Hutsel, W. A. Stygar, D. V. Rose, and Y. Maron, Experimental study of current loss and plasma formation in the *Z* machine post-hole convolute, Phys. Rev. Accel. Beams **20**, 010401 (2017).

[12] G. V. Vogman, J. H. Hammer, U. Shumlak, and W. A. Farmer, Two-fluid and kinetic transport physics of Kelvin–Helmholtz instabilities in nonuniform low-beta plasmas, Phys. Plasmas **27**, 102109 (2020).

[13] K. Tummel, C. L. Ellison, W. A. Farmer, J. H. Hammer, J. B. Parker, and K. R. LeChien, Kinetic simulations of anomalous resistivity in high-temperature current carrying plasmas, Phys. Plasmas **27**, 092306 (2020).

[14] W. A. Farmer, C. L. Ellison, J. H. Hammer, K. R. LeChien, N. B. Meezan, K. S. Raman, V. Svidzinski, and K. Tummel, Numerical improvements in magnetohydrodynamic, pulsed power simulations of near-target plasmas, IEEE Trans. Plasma Sci. 1 (2024).

[15] A. Vedenov, E. Velikhov, and R. Sagdeev, Nonlinear oscillations of rarified plasma, Nucl. Fusion **1**, 82 (1961).

[16] W. Drummond and D. Pines, Non-linear stability of plasma oscillations, Nucl. Fusion Suppl. **3**, 1049 (1962).

[17] A. A. Vedenov, Quasi-linear plasma theory (theory of a weakly turbulent plasma), J. Nucl. Energy, Part C Plasma Phys. **5**, 169 (1963).

[18] I. B. Bernstein and F. Engelmann, Quasi-linear theory of plasma waves, Phys. Fluids **9**, 937 (1966).

[19] C. F. Kennel and F. Engelmann, Velocity space diffusion from weak plasma turbulence in a magnetic field, Phys. Fluids **9**, 2377 (1966).

[20] B. V. Chirikov, A universal instability of many-dimensional oscillator systems, Phys. Rep. **52**, 263 (1979).

[21] C. F. F. Karney, Stochastic ion heating by a lower hybrid wave: II, Phys. Fluids **22**, 2188 (1979).

[22] I. Dodin, Quasilinear theory for inhomogeneous plasma, J. Plasma Phys. **88**, 905880407 (2022).

[23] J. A. Krommes, A tutorial introduction to the statistical theory of turbulent plasmas, a half-century after Kadomtsev's plasma turbulence and the resonance-broadening theory of Dupree and Weinstock, J. Plasma Phys. **81**, 205810601 (2015).

[24] D. W. Crews and U. Shumlak, On the validity of quasilinear theory applied to the electron bump-on-tail instability, Phys. Plasmas **29**, 043902 (2022).

[25] B. B. Kadomtsev, *Plasma Turbulence* (Academic Press, San Diego, CA, 1965).

[26] N. Krall and A. Trivelpiece, *Principles of Plasma Physics* (McGraw-Hill, New York, NY, 1973).

[27] S. E. Parker, C. S. Haubrich, S. Tirkas, Q. Cai, and Y. Chen, Comparison of saturation rules used for gyrokinetic quasilinear transport modeling, Plasma **6**, 611 (2023).

[28] N. Besse, Y. Elskens, D. F. Escande, and P. Bertrand, Validity of quasilinear theory: Refutations and new numerical confirmation, Plasma Phys. Control. Fusion **53**, 025012 (2011).

[29] D. F. Escande, D. Bénisti, Y. Elskens, D. Zarzoso, and F. Doveil, Basic microscopic plasma physics from N-body mechanics, Rev. Mod. Plasma Phys. **2**, 9 (2018).

[30] B. B. Chakraborty, Hydromagnetic Rayleigh–Taylor instability of a rotating stratified fluid, Phys. Fluids **25**, 743 (1982).

[31] A. Thyagaraja and K. G. McClements, Plasma physics in non-inertial frames, Phys. Plasmas **16**, 092506 (2009).

[32] J. H. Hammer, J. L. Eddleman, P. T. Springer, M. Tabak, A. Toor, K. L. Wong, G. B. Zimmerman, C. Deeney, R. Humphreys, T. J. Nash, T. W. L. Sanford, R. B. Spielman, and J. S. D. Groot, Two-dimensional radiation-magnetohydrodynamic simulations of SATURN imploding Z pinches, Phys. Plasmas **3**, 2063 (1996).

[33] J. H. Hammer and D. D. Ryutov, Linear stability of an accelerated, current carrying wire array, Phys. Plasmas **6**, 3302 (1999).

[34] F. Crawford, Cyclotron harmonic waves in warm plasmas, Radio Sci. D **69**, 789 (1965).

[35] T. Shepard, *Fast Wave Ion Cyclotron Resonance Heating Experiments on the Alcator C Tokamak* (Plasma Fusion Center, Massachusetts Institute of Technology, Cambridge, MA, 1988).

[36] G. V. Vogman, J. H. Hammer, and W. A. Farmer, Customizable two-species kinetic equilibria for nonuniform low-beta plasmas, Phys. Plasmas **26**, 042119 (2019).

[37] J. P. Freidberg and R. A. Gerwin, Lower hybrid drift instability at low drift velocities, Phys. Fluids **20**, 1311 (1977).

[38] G. V. Vogman, P. Colella, and U. Shumlak, Dory–Guest–Harris instability as a benchmark for continuum kinetic Vlasov–Poisson simulations of magnetized plasmas, J. Comput. Phys. **277**, 101 (2014).

[39] I. A. M. Datta, D. W. Crews, and U. Shumlak, Electromagnetic extension of the Dory–Guest–Harris instability as a benchmark for Vlasov–Maxwell continuum kinetic simulations of magnetized plasmas, Phys. Plasmas **28**, 072112 (2021).

[40] N. Gladd, The lower hybrid drift instability and the modified two stream instability in high density theta pinch environments, Plasma Phys. **18**, 27 (1976).

[41] R. C. Davidson, N. T. Gladd, C. S. Wu, and J. D. Huba, Effects of finite plasma beta on the lower-hybrid-drift instability, Phys. Fluids **20**, 301 (1977).

[42] M. Galvez, S. P. Gary, C. Barnes, and D. Winske, Computer simulations of plasma expansion across a magnetic field, Phys. Fluids **31**, 1554 (1988).

[43] J. D. Huba, J. F. Drake, and N. T. Gladd, Lower-hybrid-drift instability in field reversed plasmas, Phys. Fluids **23**, 552 (1980).

[44] R. C. Davidson, Quasi-linear stabilization of lower-hybrid-drift instability, Phys. Fluids **21**, 1375 (1978).

[45] A. G. Sgro, S. Peter Gary, and D. S. Lemons, Expanding plasma structure and its evolution toward long wavelengths, Phys. Fluids B **1**, 1890 (1989).

[46] I. E. Ochs and N. J. Fisch, Nonresonant diffusion in alpha channeling, Phys. Rev. Lett. **127**, 025003 (2021).

[47] J. D. Huba, N. T. Gladd, and K. Papadopoulos, The lower-hybrid-drift instability as a source of anomalous resistivity for

magnetic field line reconnection, Geophys. Res. Lett. **4**, 125 (1977).

[48] D. Winske and P. C. Liewer, Particle simulation studies of the lower hybrid drift instability, Phys. Fluids **21**, 1017 (1978).

[49] R. C. Davidson and J. M. Ogden, Electromagnetic ion cyclotron instability driven by ion energy anisotropy in high-beta plasmas, Phys. Fluids **18**, 1045 (1975).

[50] R. Davidson, *Methods in Nonlinear Plasma Theory* (Elsevier Science, Amsterdam, 2012).

[51] T. Lafleur, R. Martorelli, P. Chabert, and A. Bourdon, Anomalous electron transport in Hall-effect thrusters: Comparison between quasi-linear kinetic theory and particle-in-cell simulations, Phys. Plasmas **25**, 061202 (2018).

[52] G. Gillen, K. Gillen, and S. Guha, *Light Propagation in Linear Optical Media* (CRC Press, Boca Raton, FL, 2017).

[53] K. G. Klein, J. C. Kasper, K. E. Korreck, and M. L. Stevens, Applying Nyquist's method for stability determination to solar wind observations, JGR Space Physics **122**, 9815 (2017).

[54] A. N. Kaufman and B. I. Cohen, Theoretical plasma physics, J. Plasma Phys. **85**, 205850601 (2019).

[55] G. V. Vogman, U. Shumlak, and P. Colella, Conservative fourth-order finite-volume Vlasov-Poisson solver for axisymmetric plasmas in cylindrical (r, v_r, v_θ) phase space coordinates, J. Comput. Phys. **373**, 877 (2018).

[56] G. V. Vogman and J. H. Hammer, High-fidelity kinetic modeling of instabilities and gyromotion physics in nonuniform low-beta plasmas, Phys. Plasmas **28**, 062103 (2021).

[57] R. Z. Sagdeev and A. A. Galeev, in *Nonlinear Plasma Theory*, edited by T. M. O'Neil and D. L. Book (W. A. Benjamin, Inc. Publishers, San Francisco, CA, 1969).

[58] A. A. Galeev and R. N. Sudan, *Basic Plasma Physics. Selected Chapters. Handbook of Plasma Physics. Vol. 1 and 2* (North-Holland Publishing Company, Amsterdam, 1989).

[59] C. B. Wang and C. S. Wu, Pseudoheating of protons in the presence of Alfvénic turbulence, Phys. Plasmas **16**, 020703 (2009).

[60] T. H. Dupree, Nonlinear theory of drift-wave turbulence and enhanced diffusion, Phys. Fluids **10**, 1049 (1967).

[61] R. Z. Sagdeev, The 1976 Oppenheimer lectures: Critical problems in plasma astrophysics. I. Turbulence and nonlinear waves, Rev. Mod. Phys. **51**, 1 (1979).